

Bright, months-long stellar outbursts announce the explosion of interaction-powered supernovae

NORA L. STROTJOHANN,¹ ERAN O. OFEK,¹ AVISHAY GAL-YAM,¹ RACHEL BRUCH,¹ STEVE SCHULZE,¹ NIR SHAVIV,² JESPER SOLLERMAN,³
ALEXEI V. FILIPPENKO,^{4,5} OFER YARON,¹ CHRISTOFFER FREMLING,⁶ JAKOB NORDIN,⁷ ERIK KOOL,³ DAN A. PERLEY,⁸ ANNA Y. Q. HO,^{6,4,9} YI YANG,¹
YUHAN YAO,⁶ MAAYANE T. SOUMAGNAC,⁴ MELISSA L. GRAHAM,¹⁰ CHRISTINA BARBARINO,³ LEONARDO TARTAGLIA,^{3,11} KISHALAY DE,⁶
DAVID A. GOLDSTEIN,⁶ DAVID O. COOK,¹² THOMAS G. BRINK,⁴ KIRSTY TAGGART,⁸ LIN YAN,¹³ RAGNHILD LUNNAN,³ MANSI KASLIWAL,⁶
SHRI R. KULKARNI,⁶ PETER E. NUGENT,^{4,14} FRANK J. MASCI,¹² PHILIPPE ROSNET,¹⁵ SCOTT M. ADAMS,⁶ IGOR ANDREONI,⁶ ASHOT BAGDASARYAN,⁶
ERIC C. BELLM,¹⁰ KEVIN BURDGE,⁶ DMITRY A. DUEV,⁶ ALISON DUGAS,^{6,16} SARA FREDERICK,¹⁷ SAMANTHA GOLDWASSER,¹ MATTHEW HANKINS,⁶
IDO IRANI,¹ VIRAJ KARAMBELKAR,⁶ THOMAS KUPFER,¹⁸ JINGYI LIANG,¹ JAMES D. NEILL,⁶ MICHAEL PORTER,¹³ REED L. RIDDLE,¹⁹ YASHVI SHARMA,⁶
PHIL SHORT,²⁰ FRANCESCO TADDIA,³ ANASTASIOS TZANIDAKIS,⁶ JAN VAN ROESTEL,⁶ RICHARD WALTERS,⁶ AND ZHUYUN ZHUANG⁶

¹*Benozio Center for Astrophysics, The Weizmann Institute of Science, Rehovot 76100, Israel*

²*The Racah Institute of Physics, The Hebrew University of Jerusalem, Jerusalem 91904, Israel*

³*Department of Astronomy, The Oskar Klein Centre, Stockholm University, AlbaNova, 10691 Stockholm, Sweden*

⁴*Department of Astronomy, University of California, Berkeley, CA 94720-3411, USA*

⁵*Miller Senior Fellow, Miller Institute for Basic Research in Science, University of California, Berkeley, CA 94720, USA*

⁶*Division of Physics, Mathematics and Astronomy, California Institute of Technology, Pasadena, CA 91125, USA*

⁷*Institut für Physik, Humboldt-Universität zu Berlin, Newtonstr. 15, 12489, Berlin, Germany*

⁸*Astrophysics Research Institute, Liverpool John Moores University, Liverpool Science Park, 146 Brownlow Hill, Liverpool L35RF, UK*

⁹*Miller Institute for Basic Research in Science, University of California, Berkeley, CA 94720, USA*

¹⁰*DiRAC Institute, Department of Astronomy, University of Washington, 3910 15th Avenue NE, Seattle, WA 98195, USA*

¹¹*INAF - Osservatorio Astronomico di Padova, Vicolo dell'Osservatorio 5, 35122 Padova, Italy*

¹²*IPAC, California Institute of Technology, 1200 E. California Blvd, Pasadena, CA 91125, USA*

¹³*Caltech Optical Observatories, California Institute of Technology, Pasadena, CA 91125, USA*

¹⁴*Computational Science Department, Lawrence Berkeley National Laboratory, 1 Cyclotron Road, MS 50B-4206, Berkeley, CA 94720, USA*

¹⁵*Universite Clermont Auvergne, CNRS/IN2P3, LPC, Clermont-Ferrand, France*

¹⁶*Institute for Astronomy, University of Hawai'i, 2680 Woodlawn Drive, Honolulu, HI 96822, USA*

¹⁷*Department of Astronomy, University of Maryland, College Park, MD 20742, USA*

¹⁸*Texas Tech University, Department of Physics & Astronomy, Box 41051, 79409, Lubbock, TX, USA*

¹⁹*Caltech Optical Observatories, California Institute of Technology, 1200 E. California Blvd, Pasadena, CA 91125, USA*

²⁰*Institute for Astronomy, University of Edinburgh, Royal Observatory, Blackford Hill, Edinburgh EH9 3HJ, UK*

ABSTRACT

Interaction-powered supernovae (SNe) explode within an optically-thick circumstellar medium (CSM) that could be ejected during eruptive events. To identify and characterize such pre-explosion outbursts we produce forced-photometry light curves for 196 interacting SNe, mostly of Type II_n, detected by the Zwicky Transient Facility between early 2018 and June 2020. Extensive tests demonstrate that we only expect a few false detections among the 70,000 analyzed pre-explosion images after applying quality cuts and bias corrections. We detect precursor eruptions prior to 18 Type II_n SNe and prior to the Type Ib_n SN 2019uo. Precursors become brighter and more frequent in the last months before the SN and month-long outbursts brighter than magnitude -13 occur prior to 25% (5–69%, 95% confidence range) of all Type II_n SNe within the final three months before the explosion. With radiative energies of up to 10^{49} erg, precursors could eject $\sim 1 M_{\odot}$ of material. Nevertheless, SNe with detected precursors are not significantly more luminous than other SNe II_n and the characteristic narrow hydrogen lines in their spectra typically originate from earlier, undetected mass-loss events. The long precursor durations require ongoing energy injection and they could, for example, be powered by interaction or by a continuum-driven wind. Instabilities during the neon and oxygen burning phases are predicted to launch precursors in the final years to months before the explosion; however, the brightest precursor is 100 times more energetic than anticipated.

Keywords: Eruptive phenomena (475) – Stellar mass loss (1613) – Circumstellar matter (241) – Late stellar evolution (911) – Stellar flares (1603) – Core-collapse supernovae (304)

1. INTRODUCTION

Despite the detection of more than 2000 core-collapse supernovae (SNe) per year, the processes leading to their explosions are still not entirely understood (see, e.g., Janka et al. 2016; Müller 2016; Glas et al. 2019) and remain unobservable as they happen deep within the cores of stars in distant galaxies. However, at least for some progenitor stars, the impending core collapse seems to have direct implications for the stellar envelope. Bright optical flares have been observed in the years leading up to the SN explosion and may offer another means of probing the conditions near the surface of progenitor stars, which are, with exception of the nearest events, too faint to be detected by any telescope.

The first pre-explosion outburst was detected two years prior to the explosion of the Type Ibn SN 2006jc (Pastorello et al. 2007; Foley et al. 2007). Most precursors were observed prior to Type IIn SNe (see, e.g., Ofek et al. 2013b; Mauerhan et al. 2013; Fraser et al. 2013; Margutti et al. 2013; Tartaglia et al. 2016; Elias-Rosa et al. 2016; Ofek et al. 2016; Thöne et al. 2017; Nyholm et al. 2017; Pastorello et al. 2018; Reguitti et al. 2019), as well as prior to a broad-lined Type Ic SN (Ho et al. 2019), and possibly a SN I Ib (Strotjohann et al. 2015). This suggests that numerous types of progenitor stars can produce such flares. However, since most flares have been detected prior to Type IIn SNe, the progenitors of these relatively rare explosions are either more likely to generate such flares, or the generated flares are brighter. A systematic study by Ofek et al. (2014a) showed that precursor eruptions prior to Type IIn SNe are the rule rather than the exception. In a similar search, Bilinski et al. (2015) did not find any precursors and claim that the rate is lower, but they relied on a small SN sample.

Type IIn SNe are characterized by relatively narrow hydrogen emission lines (see, e.g., Filippenko 1997; Gal-Yam 2017; Smith 2017), which indicate the presence of a slowly moving circumstellar medium (CSM) surrounding the SN ejecta. This material originates from the star itself and is expelled in the years to decades before the explosion either during precursor eruptions or by a stellar wind. The SN ejecta crash into the CSM and a fraction of the ejecta kinetic energy is converted to high-energy photons (see, e.g., Katz et al. 2011; Murase et al. 2011, 2014). If the CSM is optically thick to gamma-ray and X-ray photons, a part of the radiation may be converted to the UV-optical regime. Some Type IIn SNe therefore reach much brighter optical peak magnitudes than noninteracting SNe (Kiewe et al. 2012; Stritzinger et al. 2012; Gal-Yam 2019) and their diverse light-curve shapes can be explained by different CSM geometries, which might

consist of several shells (see, e.g., Margutti et al. 2013; Nyholm et al. 2017) or be aspherical (Patat et al. 2011; Soumagnac et al. 2019, 2020), as is commonly observed for planetary nebulae in our Galaxy.

The progenitor stars of a few nearby Type IIn SNe were identified in archival images and are consistent with being luminous blue variables (LBVs; see, e.g., Gal-Yam et al. 2007; Gal-Yam & Leonard 2009; Foley et al. 2011; Kochanek & Szczygiel 2011). These bright and massive stars are named after their hot surface temperatures and their high-amplitude luminosity variability. They launch strong winds, which remove part of their hydrogen envelope. They were therefore traditionally considered stars in a transitional phase which evolve from a main-sequence star into a hydrogen-stripped Wolf-Rayet star (Humphreys & Davidson 1994). Another possibility is that they develop from a main-sequence star that gains mass and angular momentum from a binary companion, which turns it into an LBV rather than a red supergiant (Smith 2017).

In addition to Type IIn SNe, evidence for interaction has also been observed for several other SN classes. Type Ibn SNe explode within a helium-rich CSM and their rapid light-curve evolution might indicate that the CSM is confined to a small radius (see, e.g., Pastorello et al. 2016; Gal-Yam 2017; Hosseinzadeh et al. 2017). The spectra of Type II superluminous supernovae (SLSNe-II) often look similar to the ones of Type IIn SNe and their large radiative energy is usually attributed to strong CSM interaction (see, e.g., Gal-Yam 2019). So called flash-spectroscopy SNe exhibit narrow emission features during the first few days after their explosion; these could originate from a confined CSM shell that is flash ionized by radiation from the shock breakout and is the quickly swept up by the expanding ejecta (see, e.g., Gal-Yam et al. 2014; Khazov et al. 2016; Yaron et al. 2017; Smith 2017; Bruch et al. 2020). Type Ia-CSM SNe are thermonuclear explosions of white dwarfs that explode inside a hydrogen-rich CSM, potentially produced by a binary companion star (Hamuy et al. 2003; Dilday et al. 2012; Silverman et al. 2013; Gal-Yam 2017). In the following, we use the expression “interaction-powered SNe” to refer to all these subclasses.

A first systematic search for precursor eruptions was done by Ofek et al. (2014a) for a sample of 16 nearby Type IIn SNe using data from the Palomar Transient Factory (PTF; Law et al. 2009; Rau et al. 2009). It established that most Type IIn progenitor stars undergo one or several precursor eruptions in the last 2.5 yr before the SN and that the rate increases in the last 4 months before the explosion. However, the study was limited by the small SN sample and by the relatively sparse

144 sampling of the pre-explosion light curves. The majority of
 145 the observations were obtained in the Mould-*R* band, such
 146 that the precursor colors could not be determined.

147 Here, we build on the work by Ofek et al. (2014a) and use
 148 data from the Zwicky Transient Facility (ZTF; Bellm et al.
 149 2019; Graham et al. 2019) to systematically search for pre-
 150 cursor eruptions prior to interacting SNe, mostly of Type II
 151 SNe. Compared to PTF, ZTF has a ~ 15 times faster sur-
 152 vey speed: with its large field of view of 47 deg^2 , it moni-
 153 tors nearly the complete sky at declinations larger than -30°
 154 and smaller than 80° (Bellm et al. 2019). Since the com-
 155 missioning of the ZTF camera in fall 2017, the survey has
 156 detected more than 200 interacting SNe for which nearly 10^5
 157 pre-explosion images are available in the *g*, *r*, and *i* bands.
 158 We here search unbinned and binned light curves for pre-
 159 explosion activity. Owing to the abundant photometric data
 160 provided by the ZTF survey and the larger SN sample, we
 161 expect to detect more precursor eruptions and measure the
 162 precursor rate more precisely. Thus, we extend the previ-
 163 ous search to fainter, shorter, and less-common precursors
 164 and expect that the eruptions are better observed with data in
 165 multiple bands.

166 The paper is structured as follows. Section 2 describes
 167 the analysis and quality cuts which allow us to reduce the
 168 rate of false-positive detections. The detected precursors are
 169 described in Sec. 3 and the luminosity-dependent precursor
 170 rates are measured in Sec. 4. In Sec. 5, we show that the
 171 material ejected during most of the detected precursors can-
 172 not account for the characteristic narrow hydrogen lines in
 173 the spectra of Type II SNe. One exception is the Type Ibn
 174 SN 2019uo, described Sec. 5.3, for which the observed in-
 175 teraction can be explained by the precursor 320 days before
 176 the explosion. In Sec. 6 we consider which mechanisms
 177 might power the precursor luminosity and whether wave-
 178 driven mass loss could launch the observed precursors. Our
 179 findings are summarized in Sec. 7.

180 2. METHODS

181 The following subsections introduce the sample selection
 182 (Sec. 2.1), the forced photometry pipeline (Sec. 2.2), and the
 183 tests we perform on the pipeline (Sec. 2.3). Next, we explain
 184 how images with astrometric errors are rejected (Sec. 2.4)
 185 and how we correct the baseline offsets and rescale underes-
 186 timated error bars (Sec. 2.5). Finally, we describe how ob-
 187 servations are combined in bins (Sec. 2.6) and estimate the
 188 expected number of false detections in Sec. 2.7.

189 2.1. Sample Selection

190 The ZTF survey produces about 1 million alerts per night
 191 (Patterson et al. 2019) which are then scored by a deep-
 192 learning algorithm to identify genuine astrophysical tran-
 193 sients (Duev et al. 2019). The resulting alert stream is fil-

194 tered either by the AMPEL broker (Nordin et al. 2019; Sou-
 195 magnac & Ofek 2018) or the GROWTH “Marshal” (Kasli-
 196 wal et al. 2019) based on different science goals, such as the
 197 detection of young SNe (Gal-Yam 2019; Bruch et al. 2020)
 198 or bright transients (Fremling et al. 2020). In most science
 199 programs potentially interesting objects are identified by as-
 200 tronomers who request spectroscopy or other follow-up ob-
 201 servations. Transients brighter than magnitude ~ 19 are usu-
 202 ally first classified based on spectra from the SED Machine
 203 (Ben-Ami et al. 2012; Blagorodnova et al. 2018; Rigault et al.
 204 2019) and higher-resolution spectra might be obtained later.

205 The commissioning phase of the ZTF survey started in fall
 206 2017, while the survey officially began in spring 2018 af-
 207 ter commissioning and building reference images. To se-
 208 lect a sample of interaction-powered SNe with ZTF pre-
 209 explosion observations, we query both the Transient Name
 210 Server (TNS¹) and the private ZTF database, the GROWTH
 211 Marshal using the ZTFquery code (Rigault 2018), for tran-
 212 sients discovered since 2018 January 1 and until 2020 June
 213 24. We only consider SNe at locations that are observable by
 214 ZTF, with declinations larger than -30° . Our sample includes
 215 all objects that are classified as SNe of Type II, Ibn, Ia-CSM,
 216 or SLSNe-II by members of the ZTF team or on TNS (see,
 217 e.g., Perley et al. 2020 for details). In addition, we include
 218 objects that show flash-spectroscopy features in early-time
 219 spectra, which were identified by Bruch et al. (2020). This
 220 brings the total sample to 239 SNe.

221 An accurate localization is required to perform forced pho-
 222 tometry (see, e.g., Yao et al. 2019), and we therefore only
 223 consider objects with at least ten ZTF detections. We find
 224 that this ensures that the position is within $0.15''$ of the best
 225 position for 90% of the SNe in the ZTF coordinate system².
 226 Out of 239 SNe, 12 objects have fewer than ten ZTF detec-
 227 tions and are discarded. The remaining 227 SNe are listed in
 228 the online version of Table 1.

229 To confirm both the SN classification and the redshift, we
 230 visually inspect spectra from the ZTF Marshal as well as the
 231 TNS. We discard in total 18 objects which we cannot verify
 232 are interacting transients. For most of these objects no good
 233 spectra are available or the observed narrow lines might origi-
 234 nate from the host galaxy. For objects that are classified as
 235 SLSNe-II, we check whether they surpass a peak magnitude
 236 of -21 in any band. SNe with fainter peak magnitudes are
 237 here considered regular Type II SNe.

238 Forced photometry is obtained for all 209 remaining SNe
 239 and we apply the quality cuts as described in the following
 240 sections. After all cuts, pre-explosion observations are avail-
 241 able for 196 SNe. This remaining sample consists of 131

¹ <https://wis-tns.weizmann.ac.il/>

² A precision of $\lesssim 0.15''$ is the required threshold for forced photometry (Frank Masci, priv. comm.).

Table 1. SNe with detected pre-explosion activity

IAU name	ZTF name	SN Type	R.A. (J2000)	Dec. (J2000)	z	t_0	Separation	Comment
			(deg)	(deg)		(JD)	(arcsec)	
SN 2018eru	ZTF 18ablqehq	IIn	185.115828	41.79289029	0.03069	2458316.6	11	
SN 2018gho	ZTF 18abucxcj	IIn	246.8412533	39.1091986	0.033	2458366.4	2.8	
SN 2018hxe	ZTF 18abwlupf	IIn	221.0426466	62.89518	0.134	2458370.7	0.37	
SN 2018kag	ZTF 18acwzyor	IIn	133.951979	3.64152020	0.02736	2458466.5	6.3	
SN 2019uo	ZTF 19aadnxbh	Ibn	180.6525136	41.0616364	0.020454	2458501.2	27	
SN 2019bxq	ZTF 19aamkmxv	IIn	254.4938	78.6037	0.0139	2458555.8	0.01	
SN 2019cmy	ZTF 19aanpcep	IIn	227.2118369	40.7137261	0.0314	2458567.9	5.8	
SN 2019iay	ZTF 19abandzh	IIn	200.27061809	8.1684897	0.0406	2458656.6	7.9	
SN 2019meh	ZTF 19abclykm	SLSN-II	321.8227253	64.4164373	0.0935	2458657.3	0.04	bg AGN ^a
SN 2019gjs	ZTF 19abiszoe	IIn	224.7381972	20.0529308	0.043	2458690.7	10	
SN 2019mom	ZTF 19ablojrw	IIn	28.9021955	53.5918978	0.0488	2458690.9	–	
SN 2019njv	ZTF 19abpidqn	IIn	304.98829689	15.37745280	0.01458	2458706.9	2.9	
SN 2019fmb	ZTF 19aavyvbn	IIn	186.68196	56.0757834	0.016	2458715.8	17	t_0 uncertain
SN 2019sae	ZTF 19acahbxd	IIn	41.2693283	26.0714348	0.048	2458728.8	9.9	
SN 2019aafe	ZTF 19abzfxel	IIn	349.0686877	48.4284178	0.075	2458740.8	–	
SN 2019vkl	ZTF 19acukucu	IIn	29.1283206	18.4399406	0.064	2458808.6	–	
SN 2019vts	ZTF 19acxmnkc	IIn	98.7642676	50.434783	0.0395	2458816.9	24	
SN 2019qny	ZTF 19adannbl	IIn	53.24978869	–2.778198	0.048	2458827.0	5.7	
SN 2020iq	ZTF 20aabcemq	IIn	43.8321616	–11.4134991	0.096	2458832.6	2.5	
SN 2019yzx	ZTF 19adcxbkw	Ia-CSM	142.6721432	21.4558832	0.057	2458840.0	2.0	
SN 2019zrk	ZTF 20aacbyec	IIn	174.9475073	19.9296524	0.0362	2458889.0	14	
SN 2020dcs	ZTF 20aacqkr	IIn	183.3561586	37.6993902	0.023958	2458894.9	3.0	
SN 2020dfh	ZTF 20aasivpe	IIn	265.506694	3.2008709	0.0293	2458903.1	6.3	
SN 2020edh	ZTF 20aaswzdm	IIn	259.0999066	40.8081331	0.033	2458914.9	3.4	

NOTE—The R.A. and Dec. values represent the median coordinates of at least 10 ZTF detections. The discovery time t_0 is either the first detection time announced on TNS or a smaller value if the transient flux is visible earlier in ZTF data. The penultimate column lists the separation from the center of the host galaxy, to judge whether active galactic nucleus (AGN) activity might contribute to the pre-explosion variability. Here, we only list SNe for which pre-explosion activity is detected (see Sec. 3). The full table, containing all 227 considered SNe described in Sec. 2.1, is available online.

^aThe detected variability likely originates from AGN activity in the center of the host galaxy and not from the progenitor star (see Sec. 2.7 and 3.1 for details).

242 Type IIn SNe, 26 SLSNe-II, 20 SNe with flash-spectroscopy
 243 signatures, 12 Type Ibn SNe, and 7 SNe Ia-CSM. Table 1
 244 list the SNe for which pre-explosion activity is detected (see
 245 Sec. 3) and a full version of this table containing all initially
 246 considered 227 SNe is available online.

2.2. The Forced Photometry Pipeline

247 We perform forced photometry using the pipeline de-
 248 scribed by Yao et al. (2019) on difference images obtained
 249 from IPAC via IRSA³. Details of the ZTF image reduction
 250 are given by Masci et al. (2019) and image subtraction is
 251

252 based on the method developed by Zackay et al. (2016). We
 253 have access to images from the ZTF partnership survey (40%
 254 of the observation time) and images that became available
 255 during the third data release⁴, which includes images from
 256 the public survey (also 40% of the time) until December 2019
 257 and Caltech data (20% of the time) until December 2018.
 258 Forced photometry on more recent public or Caltech data
 259 cannot be done as the full images are not yet available.

260 The forced-photometry pipeline was implemented by Yao
 261 et al. (2019). It relies on the IPAC difference images and the
 262 measured point-spread functions (PSFs). An image cutout

³ <https://irsa.ipac.caltech.edu/Missions/ztf.html>

⁴ <https://www.ztf.caltech.edu/page/dr3>

around the SN position is produced and the background is measured within an annulus with an inner radius of 10 pixels and an outer radius of 15 pixels, where 1 pixel corresponds of 1.01'' on the sky. The median background flux is subtracted from the cutout and the 7×7 pixels around the SN position are used for the PSF fit. To quantify the uncertainty in the flux, the normalization of the PSF is fitted with a Markov chain Monte Carlo algorithm. While Yao et al. (2019) used 250 random walkers for the fit, we lower the number to 50 walkers to reduce the computation time. For 50 walkers the fitting algorithm introduces an uncertainty that is smaller than 2% of the typical error in the measured flux. We hence find that 50 walkers provide sufficient accuracy.

Based on the procedure of Yao et al. (2019) as well as our own findings, we exclude some data points from the light curves. Our exclusion criteria are as follows.

1. Images obtained early in the survey with an unknown quadrant ID for which the reference image cannot be identified.
2. Flagged difference images which might suffer from issues during the image subtraction.
3. Observations with seeing > 4''. The PSF fit is only done on the inner 7×7 pixels and might not be accurate for a very broad PSF.
4. Images affected by bad pixels at the SN position (inner 7 × 7 pixels).
5. Early *g*-band observations obtained between MJD 2,458,120 and 2,458,140, which are not well calibrated.
6. Difference images with a background standard deviation > 25 in units of detector data number (see Yao et al. 2019) which indicate problems during the image subtraction.
7. Data points with flux errors that are seven times larger than the median flux error for this SN to remove images for which the PSF fit did not converge.

These initial quality cuts remove ~ 10% of the data as shown in Table 3. We are left with 85,333 pre-explosion data points which are listed in Table 2. All fluxes are corrected for Milky Way extinction using the python package *sfdmap*, which is based on the dust map of Schlegel et al. (1998) recalibrated to the values of Schlafly & Finkbeiner (2011) and the Cardelli et al. (1989) extinction law.

2.3. Background Samples

We quantify the expected rate of false detections by performing forced photometry in locations where no precursors are expected. The four background samples are

1. empty positions in the sky close to the SN position, but outside of the host galaxy;
2. faint Gaia stars with *g*-band magnitudes between 20.5 and 18.5 close to the SN position, to identify misaligned images;
3. the SN position mirrored across the center of its host galaxy; and
4. the positions of Type II_n SNe discovered during the PTF survey before 2015.

The tests are designed such that they start from a case for which image subtraction is easy (an empty position in the image) and progress to increasingly more realistic, but challenging environments for our pipeline. The first three tests are done for the exact same images that also contain the SN positions; hence, they have the same observing conditions, reference images, and subtractions. The two last tests are considered the most realistic ones as they are performed in host galaxies or locations where Type II_n SNe explode. The second background sample is used to identify and exclude images with astrometric errors.

The positions for the background samples are generated as follows. For empty locations we randomly pick several locations at a distance of 50 pixels (i.e., 50.6'') from the SN position. Faint stars or unresolved galaxies are selected from the Gaia catalog. To reject extended sources we require an astrometric excess noise of less than 1 milliarcsec and the *g*-band magnitude is limited to values between 20.5 to 18.5 to ensure that the luminosity is similar to that of a faint precursor. Moreover, the separation from the SN position is required to be at least 20 pixels, such that the SN light does not fall within the annulus region for which the background level is calculated (see Sec. 2.2). To identify the SN host galaxies, we query the NED database for objects close to the SN position. We reject those identified as stars, the SN itself, and infrared sources, many of which are also stars (Cutri et al. 2013).

The selected empty locations, faint stars, and host-galaxy candidates are then displayed on top of the reference image for visual inspection. When selecting empty positions and stars, we check that they are isolated, located outside of the host galaxy, and are not affected by artefacts in the reference images, such as dead columns, stellar spikes, or the edge of the image. Among the host-galaxy candidates we select the most likely host. For most images, a known galaxy is consistent with the visible center of the host in the reference image, but for a few objects we select a UV source. If several NED sources are close to the center of the host we compare with multicolor SDSS images to identify the most likely center. We caution that we might not identify the true host center in

Table 2. Forced photometry pre-explosion light curves

SN name	ZTF name	JD	band	ref. im.	flux	flux err.	sys. err.	red. χ^2	red. χ^2_{star}
					10^{-10}	10^{-10}	10^{-10}		
SN 2018atq	ZTF 18aahmhxu	2458076.93147	<i>r</i>	5751232	-0.0448	8.38	1.26	0.56	0.85
SN 2018atq	ZTF 18aahmhxu	2458079.03350	<i>r</i>	5751232	6.49	11.7	1.26	0.96	1.33
SN 2018atq	ZTF 18aahmhxu	2458089.03796	<i>r</i>	5751232	6.66	8.41	1.26	1.15	1.30
SN 2018atq	ZTF 18aahmhxu	2458091.02603	<i>r</i>	5751232	-39.4	24.4	1.26	0.44	1.25
SN 2018atq	ZTF 18aahmhxu	2458091.04729	<i>r</i>	5751232	11.5	29.3	1.26	0.87	1.32

NOTE—The fifth column specifies which reference image was used (e.g. for the first rows the image for the ZTF field 575, CCD 12, quadrant 3 and filter 2, the *r* band; see also Yao et al. 2019). All fluxes have been corrected for the zeropoint and are given as a dimensionless ratio (see Eq. 8 in Yao et al. 2019). This flux ratio is also known as "maggie" (Finkbeiner et al. 2004). The third to last column lists the noise level in the reference image which is a systematic error on the measured flux. The two last columns show the reduced χ^2 of the PSF fit at the SN location as well at the location of a nearby faint star (see Sect. 2.4). The full version of the table is available online.

all cases. These positions are primarily used to build a background sample, so we do not require a high accuracy. With this method we locate the presumable centers of 160 host galaxies. The hosts of the remaining SNe are not listed in the NED database, mostly because they are faint. Some of them are even undetected in the ZTF reference images, especially for SLSNe.

The SN position is then mirrored on the location of the identified host galaxy and we verify that the two positions are sufficiently separated. The PSF fit is done for the inner 7×7 pixels — that is, the pixel containing the SN position and the three neighboring ones. However, if the seeing disk is large, the PSF of the SN could be broader. We therefore require a separation of at least 10 pixels between the actual and mirrored positions. Only 59 out of 160 SNe with identified host galaxies show a sufficiently large separation (see also Table 1). To increase the sample size, we select in addition SNe of Type II_n that were discovered during the PTF survey. We query the TNS database for publicly available SNe detected prior to 2015. A slowly developing Type II_n SN might still be detectable after ~ 3 yr, but an inspection of the ZTF light curves shows that this is not the case for any of the selected objects. Moreover, we add six objects analyzed by Ofek et al. (2014a) for which the SN was not observed by PTF. This brings the sample to a total of 104 objects out of which ZTF data are available for 100.

We produce forced photometry light curves for all selected positions to test the pipeline. The sample of Gaia stars is used in Sec. 2.4 to reject misaligned images with astrometric residuals produced during the image subtraction. The other samples are used in Sec. 2.5 to inspect the data quality and in Sec. 2.7 to estimate the rate of false-positive detections. Table 3 shows the impact of the derived cuts and corrections on the number of (false) detections and on the total number

of data points. The sample of Gaia stars is omitted in the table, because variable stars may result in actual detections.

2.4. Astrometric Errors

The large number of analyzed observations requires tight cuts on the data quality to avoid false-positive detections. Some of the reference or difference images might suffer from misalignments such that residuals are created in the image-subtraction process. Alignment errors result from several factors, including atmospheric scintillations (e.g., Osborn et al. 2015; Ofek 2019). To identify and remove affected images, we perform forced photometry at the position of a relatively faint star or an unresolved galaxy close to the SN position as described in Sec. 2.3. We choose faint stars because they roughly represent the surface brightness of bright galaxies. If the images are well aligned, no detection is expected for a nonvariable star, or for a variable star the residual should be well described by the PSF.

Images with astrometric residuals are identified via the reduced χ^2 of the PSF fit. We find that requiring a reduced $\chi^2 < 1.4$ at the position of the star removes most false detections. The corresponding difference images are flagged and are not used when searching for precursors at the SN position. In addition to misalignments, there could be more localized residuals or artefacts. We therefore require that the reduced χ^2 at the SN position is also smaller than 1.4. As shown in Table 3, these two cuts remove in total 12% of the data. The reduced χ^2 values for each data point are given in Table 2.

2.5. Offsets and Rescaling Flux Errors

As a next step, we verify that the pre-explosion light curves are centered around zero flux and that the estimated flux errors account for the observed flux scatter. When visually

Table 3. Cuts on data quality

step	# precursors / # data points			
	empty pos.	mirrored pos.	PTF SNe	real data
0 before cuts	4 / 176815	3 / 45092	116 / 48250	415 / 95442
1 known reference image	4 / 175888	3 / 44491	116 / 48067	415 / 94515
2 difference image not flagged	4 / 169522	3 / 43007	94 / 46328	399 / 91000
3 seeing $\leq 4''$	3 / 166119	3 / 42155	82 / 45292	382 / 88850
4 no bad pixels within 7×7 pixels	3 / 166119	3 / 42155	82 / 45292	382 / 88850
5 no early g -band images	3 / 165351	3 / 41988	75 / 45038	365 / 88078
6 std. of bkg. < 25	3 / 163808	3 / 40877	75 / 44349	362 / 86141
7 err. on flux < 7 times median err.	3 / 162485	3 / 40575	75 / 44054	361 / 85333
8 red. $\chi^2 < 1.4$ for nearby star	3 / 150637	3 / 37774	73 / 40740	265 / 78946
9 red. $\chi^2 < 1.4$ at SN position	2 / 148884	3 / 36888	5 / 37058	204 / 73105
10 ≥ 20 pre-expl. observations	2 / 136338	3 / 33600	4 / 36300	189 / 70420
11 offset correction	2 / 136338	9 / 33600	11 / 36300	189 / 70420
12 error-bar scaling	2 / 136338	1 / 33600	3 / 36300	136 / 70420
13 ref. sys. error / final unbinned	2 / 136338	0 / 33600	3 / 36300	152 / 70420
14 1-day bins	1 / 63791	1 / 15682	4 / 16979	124 / 32993
15 7-day bins	0 / 25528	2 / 6456	4 / 7616	84 / 14193
16 90-day bins	0 / 3983	2 / 1045	2 / 1281	37 / 2093

NOTE—Number of remaining data points and (false) 5σ detections after each step of the analysis, as described in Sec. 2.2 (steps 1 to 7), Sec. 2.4 (step 8 and 9), Sec. 2.5 (steps 10 to 12) and in Sec. 2.6 (step 13 and 14). Our actual search (last column) yields a much larger number of precursor detections than the three background samples. The initially large number of detections for the PTF sample is due to AGN activity in the host galaxy of SN 2011cc (see Sec. 2.7) and a few detections of this AGN persist after all cuts. The false detections for the empty and mirrored positions are all caused by a faulty reference image.

425 inspecting pre-explosion light curves, we find that the median
426 fluxes are sometimes systematically offset from zero. In
427 some cases, the offset could be due to light in the reference
428 image either from the transient or from a precursor. How-
429 ever, we also see such offsets for the background samples.
430 They can be as large as the typical error bar of the unbinned
431 fluxes. We therefore do a baseline correction for all light
432 curves. Consequently, we cannot identify precursors during
433 the reference period or very long-lasting precursors that af-
434 fect all data points (see also Sec. B). Moreover, we find that
435 the size of the error bars is overestimated or underestimated
436 by typically 10–20%. For a handful of locations, the errors
437 even have to be increased by as much as 50% to account for
438 the observed scatter.

439 These biases are corrected for each reference image sep-
440 arately. To do this precisely, we require at least 20 pre-
441 explosion observations with the same reference image. If
442 fewer observations are available, the corresponding data
443 points are discarded (step 10 in Table 3). After applying all
444 cuts, we find that no pre-explosion observations are left for
445 13 out of 209 SNe (see Sec. 2.1); most of them were detected

446 in the beginning of the survey (see online version of Table 1).
447 Our final sample hence consists of 196 SNe.

448 We find that using the median pre-explosion flux to cor-
449 rect the baseline does not work for all SNe, because some of
450 them have long-lasting precursors that contain close to half of
451 the data points. We therefore calculate the *iterative median*
452 which is more robust. We first combine same-night observa-
453 tions in bins to avoid individual nights with many observa-
454 tions dominating the result. Next, the median is calculated
455 for the binned data points and the data point with the largest
456 deviation from the median (regardless of the size of the error
457 bars) is removed from the sample. This last step is repeated;
458 we recalculate the median for the remaining points and re-
459 move the most distant data point, until only 30%, but at least
460 20, of the data points are left. The median of these remaining
461 points is used as the baseline correction. We find that this
462 algorithm reliably identifies the zero flux level and removes
463 the impact of any precursors during the reference period.

464 When searching for precursors at the SN positions, we se-
465 lect all objects with positive or negative 5σ detections and
466 check whether we can redo the baseline correction for a

467 time range that excludes the potential precursor, preferentially
 468 after the SN has faded. If this is possible we recal-
 469 culate the baseline correction, this time using a simple med-
 470 dian. This step leads to additional precursor detections for
 471 SNe with few pre-explosion observations (e.g., SN2018eru
 472 and SN2018kag) and improves the baseline correction for
 473 SNe for which a large fraction of the data points are part of
 474 the precursor, such as SN2019fmb (see Sec. 3.1). We also
 475 find that observations obtained after SN2019cmy had faded
 476 are systematically lower than pre-explosion observations. As
 477 discussed in Appendix B, we are not sure whether this drop
 478 in flux is due to a systematic error or an extremely bright
 479 progenitor star. In this paper, we exclude the late-time obser-
 480 vations and only discuss the short precursor detected relative
 481 to the flux level of the pre-explosion light curve (see Fig. 3).

482 Next, we scale up the flux errors if they are underestimated,
 483 which is again done for every reference image separately. As
 484 before, the result might be biased by precursors which can in-
 485 flate the error bars and remain undetected as a consequence.
 486 We therefore split the pre-explosion light curves for each refer-
 487 ence image into equal segments of 15 or more data points.
 488 We calculate the *local robust standard deviation* for each seg-
 489 ment by determining the 15.9% and 84.1% percentile and di-
 490 viding its difference by 2. The median standard deviation for
 491 all segments is used to judge whether the error bars are suf-
 492 ficiently large to account for the observed noise level. If the
 493 standard deviation is larger than 1 (i.e., the error bars can-
 494 not fully account for the observed size of the 1σ -region), the
 495 error bars are multiplied with the robust standard deviation
 496 of the median segment. No scaling is done if the standard
 497 deviation is smaller than 1 (i.e., the errors are overestimated
 498 compared to the observed scatter).

499 2.6. Binned Light Curves and the Systematic Error of the 500 Reference Image

501 To increase our sensitivity to faint precursors we also
 502 search binned light curves. The bins are chosen such that
 503 same-night observations are always combined in the same
 504 bin and the edge of the last pre-explosion bin is at the end
 505 of the night in which the SN is discovered. We ensure that
 506 data points before and after the estimated explosion date are
 507 never combined in the same bin by binning the two parts of
 508 the light curve separately. For each bin, we use the median
 509 observation date as the observation time of the bin and calcu-
 510 late the weighted mean flux and its uncertainty.

511 When combining a large number of observations in one
 512 bin, the uncertainty in the flux can become very small. How-
 513 ever, the ZTF reference images only consist of about 15 coad-
 514 ded observations; hence, the noise level in the reference im-
 515 age has to be considered. For this purpose we convert the
 516 limiting magnitude of the reference image to a flux which is
 517 given in Table 2. This systematic error is added in quadra-

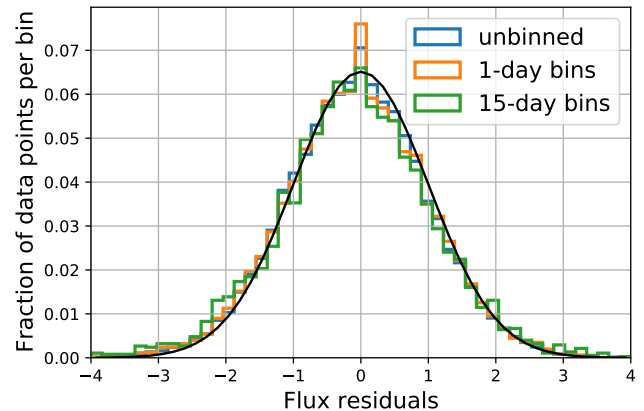


Figure 1. Flux residuals for the background sample of mirrored po-
 sitions (see Sec. 2.3) compared to a normal distribution. The base-
 lines have been centered around zero and underestimated flux errors
 have been rescaled as described in Sec. 2.5.

518 ture to the uncertainty of the unbinned or binned fluxes. It
 519 is typically ten times smaller than the uncertainty in the flux
 520 measured in a single image and thus only becomes relevant
 521 if many observations are coadded in a bin. When combining
 522 flux measurements that have different reference images we
 523 use the median systematic error.

524 We verify that the flux residuals indeed follow a normal
 525 distribution with a width of 1 by showing the flux residuals
 526 (i.e., the flux divided by its uncertainty) in Fig. 1. Except
 527 for statistical fluctuations, the residuals roughly follow a nor-
 528 mal distribution. We expect some deviations from a normal
 529 distribution, for example because we do not reduce the size
 530 of overestimated flux errors (see Sec. 2.5). For 15-day bins
 531 the systematic error in the reference image also becomes rel-
 532 evant, such that we expect a slightly narrower distribution.
 533 The distributions in Fig. 1 illustrates that only very few data
 534 points deviate from 0 by more than 3σ . This indicates that the
 535 forced-photometry pipeline and our cleaning process work
 536 well in locations where interacting SNe explode and that the
 537 error bars have an appropriate size after the scaling described
 538 in Sec. 2.5. For the precursor search we use a 5σ threshold.

539 2.7. Expected Number of False Detections and 540 Astrophysical Backgrounds

541 The empty positions as well as the mirrored positions
 542 and historic SNe serve as a quality check of the forced-
 543 photometry pipeline. We do not expect any astrophysical
 544 precursors at these positions and can therefore use these to
 545 calculate the false-alarm rate. Table 3 shows that our actual
 546 search (last column) yields 152 5σ detections for unbinned
 547 light curves even though only a few false detections are ex-
 548 pected. This gives us confidence that the majority of the de-
 549 tected precursors are astrophysical. In addition, these precur-

sors are almost exclusively detected among Type II_n SNe and they prefer low-redshift objects, as expected.

Nevertheless, a small number of false detections persist after all cuts. We inspect them to identify possible reasons. For empty and mirrored positions all false detections occur in the g -band images that contain SN 2018bih. A visual check shows that the reference image contains structures that are not astrophysical. In the actual search for this SN, we do not find any precursor candidates, potentially because only few pre-explosion images are available owing to its explosion date in May 2018. Another notable issue is the large number of detections at locations where PTF SNe exploded prior to 2015 (penultimate column in Table 3). Most of them (97 out of 116 detections before cuts) are at the position of SN 2011cc and are likely due to AGN activity close to the SN position (see below). Our cuts remove most detections at this position, but a few remain. We conclude that our precursor search might yield a few false detections, for example owing to faulty reference images and background AGNs.

A large number of false detections is found at the position of SN 2011cc, which exploded at a distance of $2.4''$ from the center of its host galaxy. The host, IC 4612, is classified as a star-forming galaxy in the SDSS catalog (Ahumada et al. 2019) and as a narrow-line AGN by Liu et al. (2011). We therefore hypothesize that the variability observed in ZTF data is caused by AGN activity. Requiring a reduced χ^2 of < 1.4 at the SN location removes most detections, because the background AGN is slightly offset from the SN position. No variability or precursors were detected in the PTF pre-explosion light curve of SN 2011cc (Ofek et al. 2014a), likely owing to the relatively small number of observations. Another case of apparent variability due to potential background AGN activity is detected in the pre-explosion light curve of SN 2019meh when searching the actual SN locations (see Sec. 3.1).

In addition, we find that light from the Type Ia SN SN 2018big contaminated the pre-explosion light curve of the flash-spectroscopy object SN 2019nmv. Both SNe happened in the same host galaxy with a separation of $3.6''$, so SN 2018big is just at the edge of the 7×7 pixel region for which the PSF fit is done (see Sec. 2.2). Since we require a small reduced χ^2 at the SN position (step 9 in Table 3), all detections of SN 2018big are rejected, such that the object does not show up as a potential precursor in the search described in Sec. 3.1. These coincidences serve as reminders that pre-explosion activity does not necessarily originate from the progenitor star, but could be related to bright, variable objects within $\lesssim 4''$.

It is also possible that a different star close to the progenitor produces precursor eruptions. It could even be the progenitor of a SN that might explode at a later time. We consider this scenario relatively rare, as no further precursors are detected

in ZTF data at 100 positions where PTF detected Type II_n SNe before 2015 (see Sec. 2.7). Nevertheless, this possibility cannot be ruled out in individual cases.

Another challenge is distinguishing between a precursor and the rising SN light curve. Double peaks or early plateaus, likely powered by shock cooling (see e.g. Sapir & Waxman 2017), have been observed for several SNe of Type Ib, Ibn and Iib (see e.g. Gal-Yam 2017). Piro & Nakar (2013) estimate that SNe powered by radioactivity can undergo a dark phase of up to several days. After this time emission from centrally located radioactive nickel-56 is able to diffuse outwards and the SN starts to rise to its main peak. We find such early detections for several SNe (e.g. for SN 2019fci). If the detection is separated by less than a week from the observed rise, we assume conservatively that the SN has already exploded at this time and adjust the discovery date t_0 accordingly. As a consequence, we might miss short-lived precursors immediately prior to the SN detection. This is especially true for objects for which the rise of the light curve is not well observed.

3. PRECURSOR PROPERTIES

After developing and testing our analysis in the previous section, here we apply it to the actual data. The detected precursors and additional tests are described in Sec. 3.1, the precursor absolute magnitude light curves and radiated energies are calculated in Sec. 3.2, and their $g - r$ colors are presented in Sec. 3.3.

3.1. Detected Precursors

To search for precursors, we produce forced photometry light curves at the SN positions and apply the cuts and corrections described in Sec. 2. Any pre-explosion data points that are significant at the 5σ level are considered detections. To gain sensitivity to fainter precursors, we search in addition the binned light curves (see Sec. 2.6). The precursor durations are unknown and moreover depend on the detection threshold. To cover a wide range of timescales we use six different bin sizes with lengths of 1, 3, 7, 15, 30, and 90 days. The bin sizes are chosen such that the amount of data approximately doubles or triples when going to the next larger bin size.

In our search of the pre-explosion data of 196 SNe, we find precursor candidates prior to 24 SNe, mostly of Type II_n; Fig. 2 indicates the number of 5σ detections in each search channel. Most precursors are detected using several different bin sizes, indicating that they are both bright and long-lasting. The precursor light curves in 1-day bins are shown in Figs. 3 and 4, and their properties are summarized in Table 4. In addition, we show coadded difference images of the precursors in Appendix A. They demonstrate that the detections are indeed due to point sources at the SN location with the exception of SN 2019sae, which might be spurious.

SN2018eru (SN IIn)				1	2	2	2
SN2018gho (SN IIn)	4	5	5	5	3	2	1
SN2018hxe (SN IIn)	1	1	1				
SN2018kag (SN IIn)	4	7	5	3	3	3	2
SN2019uo (SN Ibn)				1	1	1	1
SN2019bxq (SN IIn)	2	1	2	1	2	2	2
SN2019cmy (SN IIn)	1	2	1	2	1	1	1
SN2019iay (SN IIn)	1	1	1	1	2	2	2
SN2019meh (SLSN-II)	1	1	3	5	5	3	2
SN2019gjs (SN IIn)	5	5	5	6	8	7	3
SN2019mom (SN IIn)	1	2	1	3	1		
SN2019njv (SN IIn)		1	1				
SN2019fmb (SN IIn)	50	34	29	20	15	8	5
SN2019sae (SN IIn)							1
SN2019aafe (SN IIn)	5	5	6	4	3	3	2
SN2019vkl (SN IIn)	13	11	13	10	9	5	2
SN2019vts (SN IIn)					3	3	2
SN2019qny (SN IIn)	2	2	2	2	3	3	3
SN2020iq (SN IIn)			1		1	1	1
SN2019yzz (SN Ia-CSM)		1	1				1
SN2019zrk (SN IIn)	57	38	21	12	6	4	2
SN2020dcs (SN IIn)	4	5	4	4	3	2	1
SN2020dfh (SN IIn)	1		1	1	1	1	1
SN2020edh (SN IIn)		2	3	3	2	2	
	unbinned	1 day	3 days	7 days	15 days	30 days	90 days

Figure 2. Number of pre-explosion detections above the 5σ threshold for each bin size. Observations in different photometric bands are binned separately and the white numbers indicate the total number of detections in all three bands. Dark-green fields represent securely detected precursors, while light-green fields mark unconfirmed precursors that are only seen in a single bin and band (see text). Orange fields signal that the flux variability is likely caused by AGN activity in the host galaxy and not by the progenitor star.

Marginally detected precursor candidates are inspected in more detail, to test whether they are genuine. For precursors that are only detected in a single bin, we check whether fluxes in the three bins before or after the detection surpass the 3σ significance threshold or whether reducing the bin size leads to at least two data points above the 3σ threshold. If we do not find any additional 3σ detections, we conclude that the detection is driven by data collected within a single night and band and refer to these detections as *unconfirmed precursors*. The light-green color in Fig. 2 highlights the four precursors that do not pass this test (the Type IIn SN 2018hxe, SN 2019njv, and SN 2019sae, and the Type Ia-CSM SN 2019yzz). The fact that we did not find any false 5σ detections when searching the background samples in Sec. 2.3 suggests that at least some of the unconfirmed precursors are astrophysical nonetheless. In the following we only focus on the 19 securely detected precursors.

One pre-explosion light curve, prior to SN 2019meh, shows long-term up-and-down fluctuations as expected for AGNs (see Fig. 3). Indeed, the SN is located within $1''$ of the center of its host galaxy and we therefore conclude that the variability is likely due to nuclear activity and is not caused by the progenitor star, as described for SN 2011cc in Sec. 2.7. SN 2019meh is a SLSN of Type II located at a relatively high (for our sample) redshift of 0.0935. Such a distant progen-

itor star would have to reach an extreme luminosity to be detectable, which supports the hypothesis that we are seeing AGN activity rather than stellar flares. We therefore remove this object from the sample.

We also check whether shifting the bin positions leads to the detection of additional precursors. For this purpose, we repeat the search with 7-day bins six times while moving the bin edges by one day for each new search. We detect precursors prior to a few SNe that are not found with the original 7-day bins, but all additional SNe already have detected precursors when using smaller or larger bins (see Fig. 2). We thus conclude that the bin positions only have a minor influence on the results.

We summarize that we securely detect pre-explosion outbursts prior to 18 different SNe of Type IIn and prior to the Type Ibn SN 2019uo (see Fig. 2). Figures 3 and 4 show that some SNe, such as SN 2018eru, SN 2019bxq, SN 2019mom, or SN 2020edh, might undergo several separate precursor eruptions. It is, however, also possible that the detections are part of a single flaring episode that lasts for several hundred days.

3.2. Precursor Energy

To put the precursor eruptions into context, we calculate the absolute magnitude light curves and estimate the radiated energies of the securely detected precursors found in Sec. 3.1. Fluxes are converted to “*asinh magnitudes*,” also called “*luptitudes*,” with a softening parameter of 10^{-10} as defined by Lupton et al. (1999). Magnitude errors are given as $\sigma_{\text{mag}} = 1.0857 \log(f/\sigma_{\text{flux}})$, where f and σ_{flux} are the dimensionless normalized fluxes and uncertainties shown in Figs. 3 and 4. The 5σ limiting magnitude is calculated as $m_{\text{lim}} = -2.5 \log(5 \times \sigma_{\text{flux}})$ and the significance of a detection is given as f/σ_{flux} . All calculations are here done for 7-day bins and we consider 3σ detections significant if they are part of a previously detected precursor. For data points that do not reach the 3σ threshold we calculate 5σ upper limits.

Figure 5 shows the resulting absolute magnitude *r*-band light curves (dashed lines indicate that the *g* band was used instead for SN 2018gho, SN 2018kag, SN 2019bxq, SN 2020edh, and the early detection of SN 2018eru). For clarity we omit nondetections that do not directly constrain the precursor duration. Most precursors are detectable for several weeks and some of them start more than 100 days before the explosion. The peak magnitudes vary between -13 and -17.5 as also summarized in Table 4. For comparison we add the *r*-band light curve measured for the 2012a event observed immediately prior to the likely final explosion of SN 2009ip (data taken from Margutti et al. 2013, Prieto et al. 2013, and Pastorello et al. 2013). Its duration, peak magnitude, and shape are similar to those of several of the less energetic precursors found in this search. We hence conclude

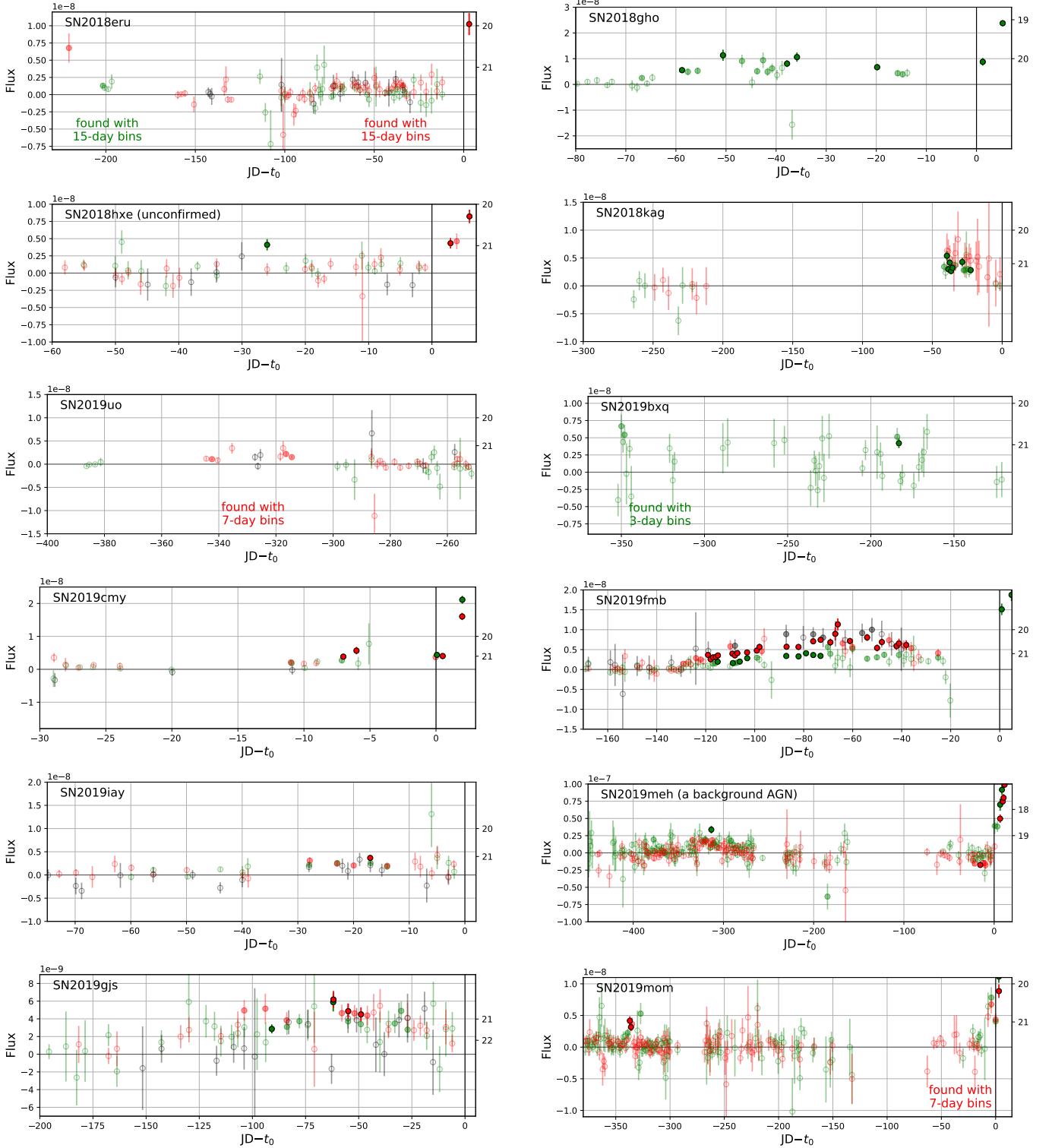


Figure 3. Precursor light curves in 1-day bins. Solid circles mark 5σ detections, circles filled with a lighter shade and without a black edge have significance between 3σ and 5σ , and open points are less significant. Green, red, and black data points were obtained in the g , r , and i bands, respectively. The vertical black line indicates t_0 , a rough estimate for the explosion date, and colored areas identify precursors that are detected significantly when using larger bins. The flux f is given as a unitless ratio relative to the zeropoint which is equivalent to the unit “maggie” used in SDSS catalogs (Finkbeiner et al. 2004). Corresponding AB magnitudes are given on the right-hand ordinate axis and are calculated as $m_{AB} = -2.5 \log_{10}(f)$.

729 that bright and long-lasting precursors are common in the last
730 months before the explosion of Type II_n SNe. Their rate is
731 quantified in Sec. 4.

732 Next, we calculate the precursor energies by integrating
733 the fluxes per bin from the first to the last detection, even if
734 individual data points in between are not significant at the
735 3σ level. The calculation is done for each band separately
736 and gaps in the data are interpolated if one or two 7-day bins
737 are empty, such as for SN 2018gho (see Fig. 3). This inter-
738 polation increases the total energy by at most 30% and thus
739 does not have a major impact on the results. We obtain sim-
740 ilar results for 3-day bins and thus conclude that the energy
741 estimates in Table 4 roughly describe the observed precur-
742 sor energy. These are lower limits on the true radiated ener-
743 gies of the precursors, which are often only partially detected,
744 and also radiate outside of the visible-light bands which we
745 cover. The brightest precursors reach radiative energies close
746 to 10^{49} ergs, about 10% of the total radiative energy in a typ-
747 ical SN explosion.

748 3.3. Precursor Colors

749 Here, we calculate the $g - r$ color index for precursors that
750 have observations in both bands. For this purpose we select
751 all bins in which a significance of 3σ is reached in at least one
752 band. If the detection in the second band is less significant we
753 quote lower or upper limits accordingly. The resulting colors
754 are shown in Fig. 6. Compared to young SNe, the precursors
755 exhibit quite red colors, which correspond to lower effective
756 temperatures. We caution, however, that the $H\alpha$ line falls
757 within the r band. The spectrum of the precursor prior to
758 PTF 13efv showed relatively strong, narrow hydrogen lines
759 (Ofek et al. 2016), and the same is true for Type II_n SNe and
760 LBV outbursts. A red color could therefore be mimicked by
761 a blue continuum flux with a strong $H\alpha$ line. The precursor
762 prior to SN 2019fmt is also detected in the i band and shows
763 a mean $g - i$ color of 1.1 mag. This corresponds to an effec-
764 tive temperature of ~ 4300 K, similar to the result from the
765 $g - r$ color index shown in Fig. 6. For this object, at least,
766 we conclude that the rather low effective temperature is not
767 primarily due to a strong $H\alpha$ line.

768 We also show the effective temperatures of the 2012a out-
769 burst of SN 2009ip in Fig. 6. They were obtained by fitting a
770 blackbody continuum to the multiband photometry (Margutti
771 et al. 2013) and are therefore less susceptible to line fluxes.
772 The precursor of SN 2009ip is slightly hotter than most pre-
773 cursors observed in our sample, and we find that the precur-
774 sors detected here typically do not cool down as observed
775 for the 2012a event prior to the final explosion of SN 2009ip
776 (Margutti et al. 2013).

777 The bolometric luminosity of the precursor L and its tem-
778 perature T can be used to estimate the radii of the photo-
779 sphere via the Stefan-Boltzmann law $R = (L/4\pi\sigma_B)^{0.5}T^{-2}$,

780 where σ_B is the Stefan-Boltzmann constant. A faint and hot
781 precursor (with a temperature of 8,000 K and an r -band mag-
782 nitude of -13) would have a small radius of $\sim 4 \times 10^{13}$ cm,
783 while a bright and cool precursor (4,000 K and a magnitude
784 of -17) would have a radius of $\sim 10^{15}$ cm. Most detected
785 precursors have photospheric radii of a few times 10^{14} cm, if
786 their emission can be described with a blackbody spectrum.
787 These large radii suggest that we cannot see down to the sur-
788 face of the progenitor star.

789 4. PRECURSOR RATES

790 Here we focus on the whole sample of pre-explosion light
791 curves and use it to calculate precursor rates. Except for one,
792 all confirmed precursors are found prior to Type II_n SNe and
793 we therefore first describe the rate for this SN class in Sec. 4.1
794 and Sec. 4.2. Precursor rates for other types of possibly in-
795 teracting SNe are presented in Sec. 4.4.

796 4.1. Precursor Rates for Type II_n SNe

797 The rate calculation is done for 7-day bins, because this
798 search channel is sensitive to faint precursors without losing
799 short precursors (see Fig. 2). Another advantage of using
800 7-day bins is that they partly compensate for differences be-
801 tween light curves obtained by the private and public surveys,
802 which have typical cadences of one day and three days, re-
803 spectively. None of the unconfirmed precursors is detected
804 for 7-day bins, so they do not enter the rate calculation.

805 The precursor rate is here defined as the fraction of time
806 during which precursors are observed above a certain limit-
807 ing magnitude. As a result, we do not distinguish between
808 two 1-week long precursors and a single precursor that lasts
809 for two weeks. The rate depends on the absolute magnitude
810 of the precursors and we calculate it in steps of 0.25 mag.
811 For each absolute magnitude we select all pre-explosion bins
812 with a deeper limiting magnitude. We then calculate which
813 fraction of these bins have precursor detections. Conse-
814 quently, precursors detected with a high significance (i.e., a
815 large difference between its magnitude and the limiting mag-
816 nitude of the bin) may contribute in several magnitude bins.
817 On the other hand, detections just at the 5σ threshold may
818 not contribute at all, if they fall in between the magnitude
819 steps⁵. The resulting rate is cumulative, as we search for
820 precursors that are brighter than the corresponding magni-
821 tude threshold. The 95% uncertainty associated with the rate
822 is calculated using the Wilson binomial confidence interval
823 (Wilson 1927; Wallis 2013) as implemented in the *astropy*
824 package (Robitaille et al. 2013; Price-Whelan et al. 2018).

⁵ For example, a precursor detected with an absolute magnitude of -14.2 and with a limiting magnitude of -14.1 would not count as a detection in the bin at magnitude -14.25 because it is not bright enough. In the next fainter bin at a magnitude -14 it also does not contribute because the limiting magnitude is not sensitive enough.

Table 4. Detected precursors

	band	start phase	end phase	median flux	energy	v_{CSM}	$\epsilon M_{\text{CSM, pre.}}$	t_{rise}	$M_{\text{CSM, diff.}}$
		(days)	(days)	(mag)	(10^{46} ergs)	(km s^{-1})	(M_{\odot})	(days)	(M_{\odot})
SN 2018eru	<i>g</i>	−202.2	−195.2	−13.3	4	1100	0.02	–	–
	<i>g</i>	−69.2	−62.2	−13.3	4				
	<i>r</i>	−76.2	−34.2	−13.4	23				
SN 2018gho	<i>g</i>	−63.0	−14.0	−15.2	160	210	4	13	< 1.3
SN 2018kag	<i>g</i>	−48.1	−20.1	−14.3	40	1100	0.04	–	–
	<i>r</i>	−41.1	−20.1	−14.7	50				
SN2019uo	<i>r</i>	−342.8	−307.8	−13.0	17	880	0.007	8	< 0.8
SN 2019bxq	<i>g</i>	−349.4	−342.4	−13.0	3	330	0.06	18	< 1.8
	<i>g</i>	−188.4	−181.4	−12.9	3				
SN 2019cmv	<i>g</i>	−13.4	−6.4	−13.9	7	150	1.1	8	< 0.8
	<i>r</i>	−13.4	−6.4	−14.6	30				
SN 2019fmb	<i>g</i>	−125.3	−27.3	−12.9	40	990	0.08	–	–
	<i>r</i>	−174.3	−20.3	−13.3	80				
	<i>i</i>	−111.3	−41.3	−14.1	80				
SN 2019iay	<i>g</i>	−34.2	−13.2	−14.7	40	340	0.4	9	< 0.9
	<i>r</i>	−34.2	−13.2	−14.8	50				
SN 2019gjs	<i>g</i>	−97.2	−20.2	−15.3	300	320	3	7	< 0.7
	<i>r</i>	−104.2	−20.2	−15.6	300				
	<i>i</i>	−55.2	−48.2	−15.5	30				
SN 2019mom	<i>g</i>	−342.5	−335.5	−14.7	13	590	0.19	–	–
	<i>r</i>	−342.5	−335.5	−15.1	19				
	<i>g</i>	−6.5	0	−16.0	50				
	<i>r</i>	−6.5	0	−16.0	50				
SN 2019aafe	<i>g</i>	−20.4	−6.4	−16.9	300	1100	0.9	4	< 0.4
	<i>r</i>	−97.4	−6.4	−16.1	1000				
SN 2019vkl	<i>g</i>	−62.2	−6.2	−16.0	500	770	1.3	10	< 1.0
	<i>r</i>	−83.2	−6.2	−16.1	800				
SN 2019vts	<i>g</i>	−41.5	−20.5	−14.6	40	340	1.2	–	–
	<i>r</i>	−62.5	−6.5	−14.9	140				
SN 2019qny	<i>g</i>	−104.6	−90.6	−15.4	50	350	2	25	< 2.5
	<i>r</i>	−125.6	−62.6	−15.4	300				
SN 2020iq	<i>r</i>	−482.2	−454.2	−15.9	170	160	7	–	–
SN 2019zrk	<i>g</i>	−55.5	−6.5	−16.2	500	350	5	7	< 0.7
	<i>r</i>	−111.5	−6.5	−16.1	700				
SN 2020dcs	<i>r</i>	−34.4	−6.4	−15.1	90	180	3	14	< 1.4
SN 2020dfh	<i>r</i>	−34.6	−20.6	−15.2	40	200	1.1	–	–
SN 2020edh	<i>g</i>	−692.5	−545.5	−13.0	80	600	0.2	–	–

NOTE—Properties of the detected precursors and the SNe. The first columns list the beginning and end of precursors with respect to t_0 , the median magnitudes and precursor energies. The CSM velocity is derived from the median width of narrow lines and P Cygni profiles (see Sec. 5.1) and is used to estimate the CSM mass multiplied by an unknown efficiency factor ϵ . t_{rise} quantifies how many days it takes the SN to rise by a factor of e (1.086 mag) to its peak in the r band (g band used for SN 2018gho and SN 2019iay). The rise time provides a rough upper limit on the total CSM mass given in the last column (see Sec. 5.2).

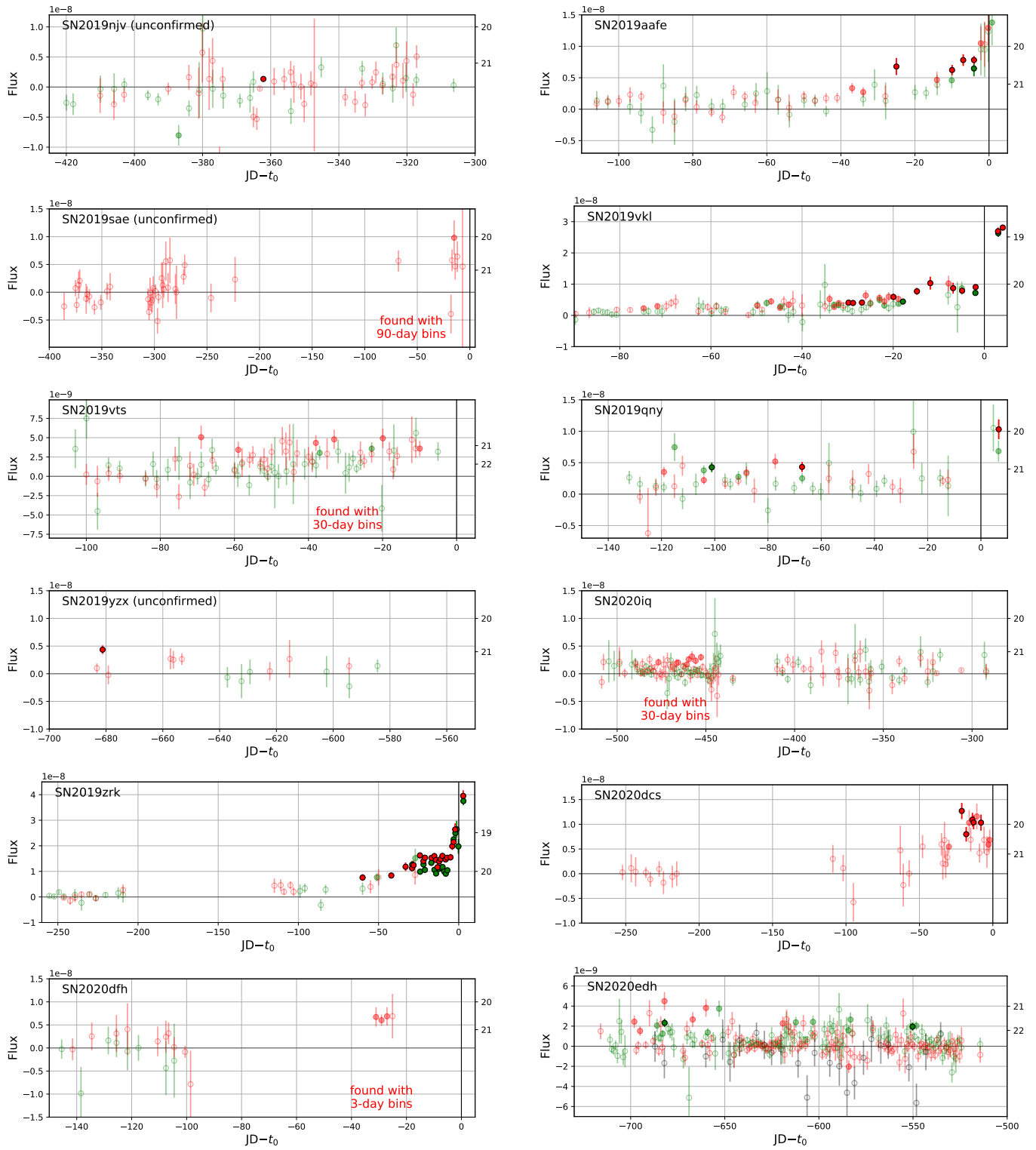


Figure 4. Precursor light curves – continuation of Fig. 3

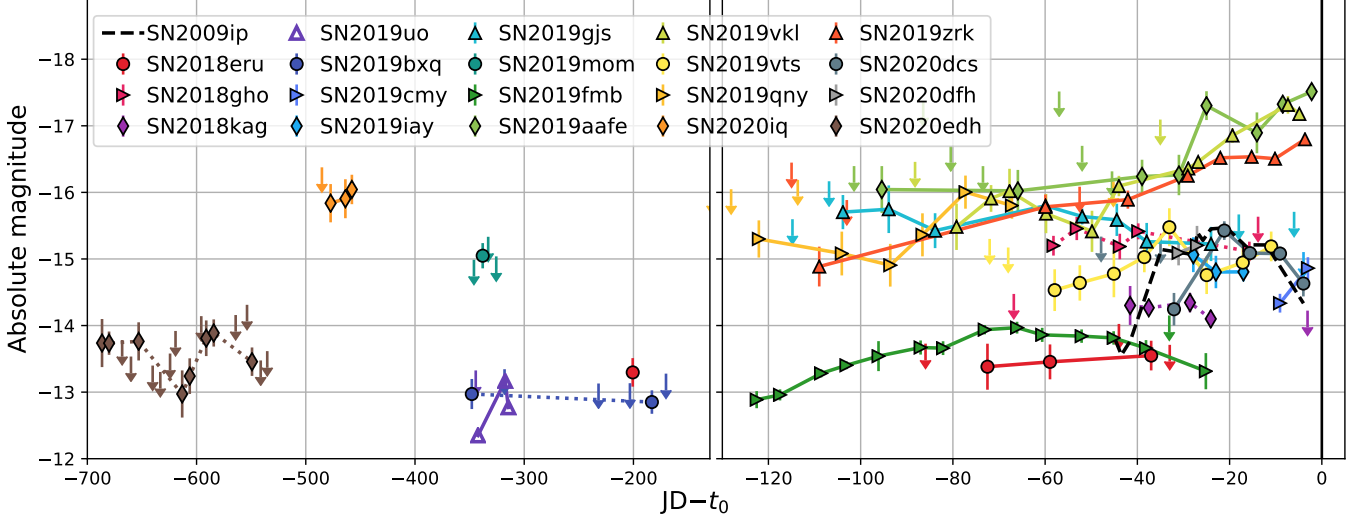


Figure 5. Absolute magnitude precursor light curves in 7-day bins. All SNe are of Type II_n, except for the Type Ib_n SN 2019uo (open markers). If available, we show the *r*-band light curve, and dotted lines indicate that the *g*-band light curves are depicted for SN 2018gho, SN 2018kag, SN 2019bxq, SN 2020edh, and the early detection of SN 2018eru. For clarity, only the most relevant nondetections are displayed. The 2012a event prior to the likely final explosion of SN 2009ip is shown as a black dashed line for comparison (light curve taken from Margutti et al. 2013, including data from Prieto et al. 2013 and Pastorello et al. 2013).

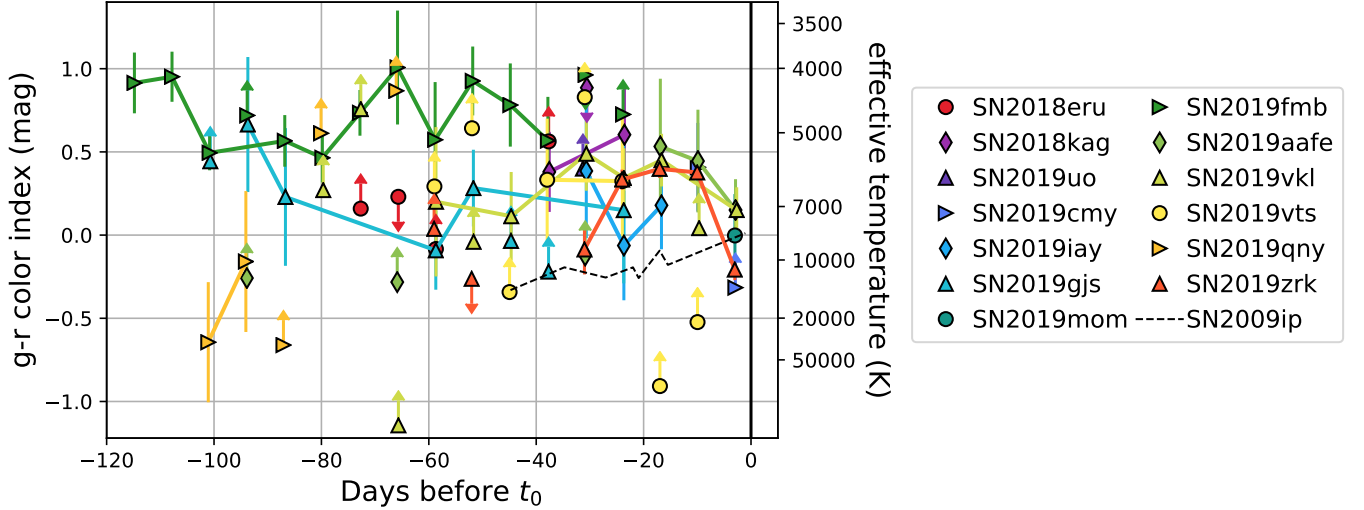


Figure 6. Color index of precursors observed in the *g* and *r* bands. The light curves are binned in 7-day bins and we quote 3σ lower or upper limits instead of detections if the *g*-band or *r*-band flux is not significant at the 3σ level.

825 The main panel of Fig. 7 shows the fraction of time during
 826 which precursors are detected for Type II_n SNe as a function
 827 of the absolute magnitude. The green, red, and gray shaded
 828 regions correspond to the parameter space that is allowed at
 829 the 95% confidence level for the *g*, *r*, and *i* bands (respec-
 830 tively), and the solid lines depict the cumulative precursor
 831 rate. For bins without detections (e.g., for bright absolute
 832 magnitudes) the colored area reaches down to zero and its
 833 upper edge corresponds to a 95% upper limit.

834 As shown in the main panel of Fig. 7, *g*-band and *r*-band
 835 precursors are detected with absolute magnitudes ranging
 836 from -17 to -12 . The rate is slightly lower in the *g* band,
 837 because of the red precursor colors observed in Sec. 3.3.
 838 The fraction of time during which we observe bright precus-
 839 sors with an absolute *r*-band magnitude of -16 or brighter
 840 is $\sim 0.7\%$ with a 95% confidence range of 0.4% to 1.2%.
 841 For fainter magnitudes, the rate increases and reaches $\sim 12\%$
 842 ($6\text{--}23\%$) for precursors brighter than magnitude -13 . The
 843 measured rates are also summarized in Table 5.

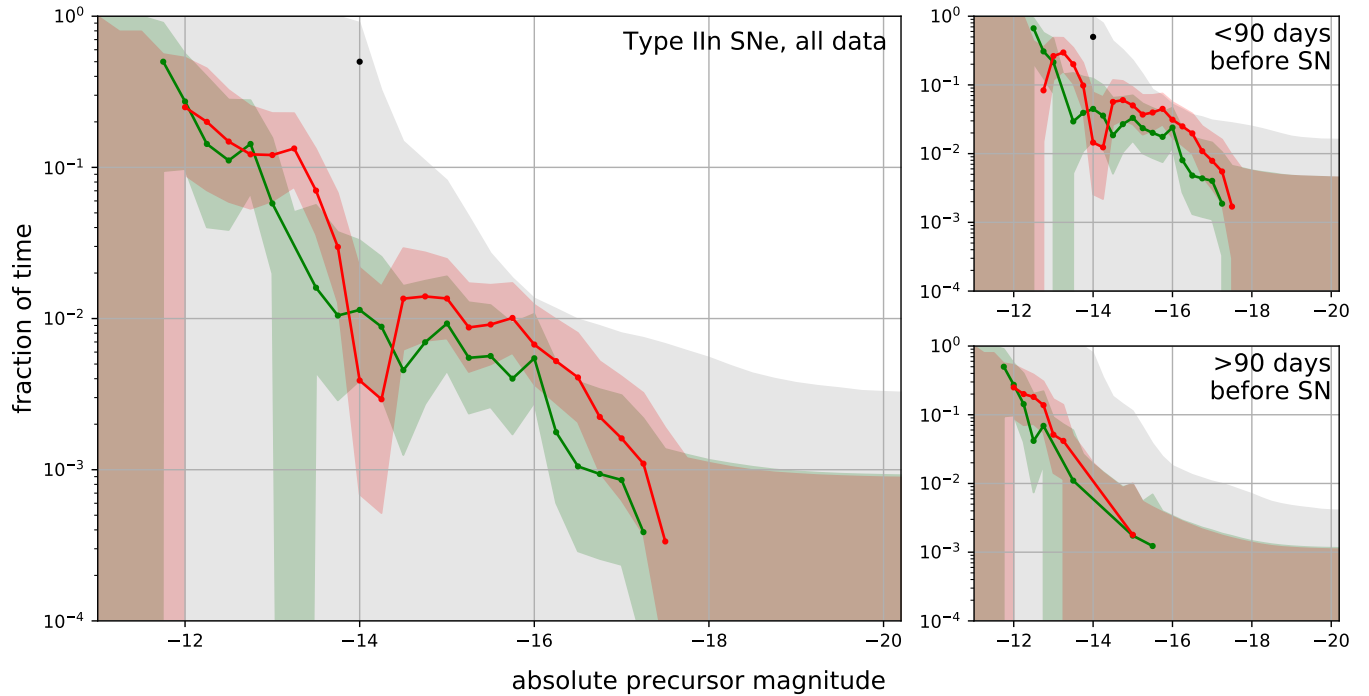


Figure 7. Fraction of time during which precursors brighter than the respective absolute magnitude are observed for Type IIh SNe. The lines show the measured rates and the shaded area indicates the 95% confidence region. If it reaches down to zero, its upper edge should be interpreted as an upper limit; otherwise it corresponds to the 95% error bar on the rate. The calculation was done for 7-day bins; the green, red, and black colors show the rates for the g , r , and i bands, respectively. The i -band precursor rate is only measured at magnitude -14 , as indicated by the black dot. In the main panel, the median phase of the observations is ~ 6 months prior to the explosion, while it is 1.4 months and 10.4 months (respectively) for the two right panels. The r -band precursor rate measured in the last 90 days before the SN explosion (upper small panel) is typically 5 times larger than the 95% upper limit on the rate measured at earlier times (lower small panel).

844 We caution that r -band precursors fainter than magnitude
 845 -14 are only detected for SN 2019fmb, so the rate of such
 846 faint precursors is determined by this object and by the fact
 847 that few other SNe have as constraining observations. The
 848 g -band rate is more robust, since such faint precursors are
 849 detected for four different SNe. The dip in the r -band rate
 850 at magnitude -14 is likely a statistical fluctuation caused by
 851 the relatively small number of SNe with precursors. The gray
 852 shaded region indicates that the i -band observations are typi-
 853 cally not sensitive enough to detect precursors. The reason
 854 is that fewer observations were obtained and they have in ad-
 855 dition larger error bars, in part owing to the lower quantum
 856 efficiency in this wavelength range for the ZTF CCD (Bellm
 857 et al. 2019). A black dot marks the only i -band detection, a
 858 precursor with magnitude -14 prior to SN 2019fmb.

859 4.2. Time Dependence of the Precursor Rate for SNe IIh

860 The rate calculation in the left-hand panel of Fig. 7 was
 861 done using all pre-explosion data that were collected over a
 862 period of up to 2.5 yr before each SN explosion. The median
 863 phase of the pre-explosion light curves is 267 days (nearly
 864 nine months) before the discovery date t_0 . The precursor light
 865 curves in Fig. 5 show that most precursors are detected in the
 866 final few months before the SN explosion. To quantify the

867 time dependency, we split the dataset into two parts: observa-
 868 tions collected within 90 days before the estimated explosion
 869 date (with a median of 42 days) and observations collected
 870 earlier (at a median time of 317 days before the SN). We then
 871 repeat the rate calculation and display the results in the two
 872 side panels of Fig. 7.

873 The r -band 95% confidence regions in the two smaller
 874 panels of Fig. 7 do not overlap for absolute magnitudes
 875 > -14.5 and the precursor rate is significantly larger in the
 876 final 90 days before the explosion. The measured rate in the
 877 final months before the explosion is up to 12 times larger
 878 than the 95% upper limit on the precursor rate before that.
 879 In the r band, the median difference for all magnitude bins
 880 between magnitude -13 and -17.5 is a factor of 5 (i.e.,
 881 the precursor rate at early times is typically more than 5
 882 times smaller). The difference would be even larger when
 883 dividing the dataset at 120 days, because several of the de-
 884 tectations in the lower-right panel of Fig. 7 are part of the
 885 > 100 -day long precursors (e.g., prior to SN 2019fmb and
 886 SN 2019gjs; see Fig. 5). The large number of precursor de-
 887 tectations shortly prior to the explosion is hence not caused by
 888 the larger amount of data available at these times, but is a
 889 genuine and significant difference.

Table 5. Precursor rates

sample	band	number of SNe	median phase	rate of bright pre. (≤ -16 mag)	rate of faint pre. (≤ -13 mag)
			(months)	(%)	(%)
Type II _n , all data	<i>g</i>	122	-8.7	0.5 (0.3 – 1.1)	6 (2 – 15)
	<i>r</i>	126	-8.8	0.7 (0.4 – 1.2)	12 (6 – 23)
	<i>i</i>	49	-9.0	< 1.4	–
Type II _n , ≤ 90 days before SN	<i>r</i>	107	-1.3	3 (1.7 – 6)	26 (12 – 49)
Type II _n , > 90 days before SN	<i>r</i>	121	-10.4	< 0.3	5 (1.4 – 17)
bright Type II _n (peak mag. < -18.5)	<i>r</i>	84	-8.5	2 (1.2 – 4)	< 79
faint Type II _n (peak mag. > -18.5)	<i>r</i>	33	-8.4	< 0.4	12 (6 – 12)
Type Ib _n	<i>r</i>	11	-8.6	< 1.4	< 38
SLSNe-II	<i>r</i>	24	-8.4	< 81	–
flash-spectroscopy SNe	<i>r</i>	20	-4.4	< 0.7	< 3.7
Type Ia-CSM	<i>r</i>	7	-7.2	< 6.9	–

NOTE—Fraction of time during which bright or faint precursors are observed with the 95% confidence range given in parentheses. If no precursors are detected the 95% upper limit is quoted instead. The calculation was done for 7-day bins and the numbers are taken from Figs. 7, 9, and 10. The number of SNe with data is given in the third column, and the fourth column lists the median phase of the pre-explosion observations which is close to nine months for most subsamples. Dashes indicate that no data are available, so the rate remains unconstrained (e.g., the rate of faint precursors in the *i* band).

890 In the three months before the explosion, faint precursors
 891 with an *r*-band magnitude of > -13 are observed 26% of the
 892 time (with a 95% confidence range of 12–49%; see also Ta-
 893 ble 5), while the rate is 5% (1.4–17%) at earlier times. The
 894 time dependence of the rate is even stronger for brighter pre-
 895 cursors with absolute magnitudes > -16 : their rate is 3%
 896 (1.7–6%) in the three months before explosion, while it is
 897 $< 0.3\%$ prior to that. We conclude that precursors become
 898 brighter and more frequent in the final months leading up to
 899 the explosion.

900 Early precursors are only observed prior to five SNe (see
 901 Fig. 5) and they appear to be fainter and short-lived compared
 902 to the precursors immediately before the explosion that typ-
 903 ically last for several months. The rate calculation in Fig. 7
 904 shows that this effect is real and not caused by a smaller num-
 905 ber of observations at early times. The luminosity increase
 906 likely continues within the last three months before the ex-
 907 plosion as shown in Fig. 5.

908 While we so far constrained the fraction of time during
 909 which precursors are observed, we here calculate in addi-
 910 tion the fraction of progenitor stars that undergo long-lasting
 911 precursors within 90 days before the SN explosion. For this
 912 purpose, we compile a sample of SNe for which such precursors
 913 are detectable. We bin the light curves in 30-day bins
 914 and require that at least two bins contain data (i.e., that ob-
 915 servations are available in two out of three months). If this
 916 condition is met, we estimate down to which limiting mag-

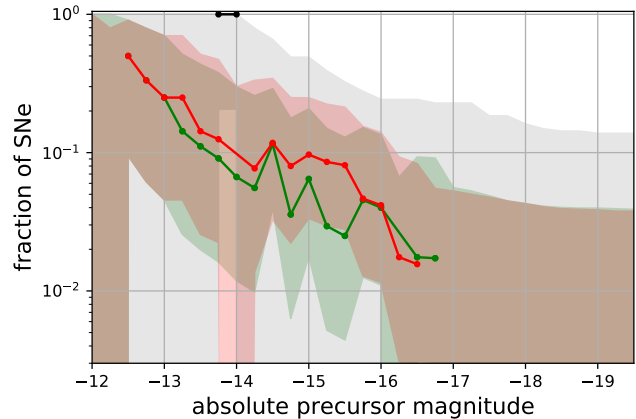


Figure 8. Fraction of Type II_n SNe with long-lasting (≥ 30 days) precursors within 90 days prior to their explosion. The lines mark measured rates and the shaded area indicates the 95% confidence regions.

917 nitude a precursor can be detected. For this purpose we use
 918 the second lowest limiting magnitude — that is, the median
 919 for three data points or the least constraining bin for two data
 920 points. The rate is then calculated for each magnitude bin
 921 by dividing the number of detected precursors by the number
 922 of light curves for which such a precursor would have been
 923 detectable.

924 The fraction of SNe with long-lasting precursors in the
 925 last three months before the explosion is shown in Fig. 8.

926 Long-lasting precursors brighter than magnitude -16 occur
 927 for about 4% (1.1–14%, 95% confidence range) of the SNe
 928 in the r band, while fainter precursors with an absolute mag-
 929 nitude brighter than -13 occur for 25% (5–69%) of the Type
 930 IIn SNe.

931 We hence conclude that precursor eruptions brighter than
 932 magnitude -13 occur prior to many, but not all Type IIn SNe.
 933 This result is in tension with some of the findings by Ofek
 934 et al. (2014a), who calculate that the average Type IIn pro-
 935 genitor undergoes several precursors brighter than magnitude
 936 -14 in the last year before its explosion. Based on this they
 937 estimate that $> 52\%$ of all Type IIn SNe exhibit at least one
 938 bright precursor in the final four months before the explosion
 939 at a confidence level of 99%. Ofek et al. (2014a) calculate
 940 the precursor rate by dividing the number of precursors by
 941 the time during which such precursors are detectable, the so-
 942 called “control time.” However, if the light curve has gaps,
 943 the control time (and thus the rate) depends on the bin size
 944 while the number of precursors does not change, as long as
 945 the bin size is smaller than their duration. To avoid such a
 946 dependence on the bin size, we calculate instead the frac-
 947 tion of bins with precursors or the fraction of well-observed
 948 SNe with precursors. The rate calculation used by Ofek et al.
 949 (2014a) and Strotjohann et al. (2015) are thus only valid if
 950 each light-curve bin contains observations.

951 Our results are likely consistent with the findings of Bilin-
 952 ski et al. (2015), who did not detect any precursors for a sam-
 953 ple of five Type IIn SNe and one SN imposter. They report
 954 that a precursor similar to the 2012a event prior to the ex-
 955 plosion of SN 2009ip would have been detectable for two
 956 of their objects. We measure that $\sim 10\%$ of all Type IIn
 957 SNe have precursors as bright as magnitude -15 (see Fig. 8)
 958 which is consistent with their non-detections. Bilinski et al.
 959 (2015) do not quote a control time, so we cannot compare to
 960 all of their results.

961 We conclude that the precursor rate increases by a factor of
 962 more than six within the last three months before the SN ex-
 963 plosion compared to earlier observations obtained on average
 964 ten months before the SN. While the rate of faint precursors
 965 (with an r -band magnitude of -13) increases by a factor of
 966 ~ 5 , the difference is more than a factor of 10 for bright pre-
 967 cursor with an r -band magnitude of brighter than -16 . Our
 968 observations do not constrain the rate of long-lasting precursors
 969 that are fainter than magnitude -13.5 . It is hence possi-
 970 ble that all progenitors of Type IIn SNe exhibit precursors if
 971 at least one third of them is fainter than this threshold.

972 4.3. Precursor Rates for Faint and Bright SNe IIn

973 Type IIn SNe can have diverse peak luminosities and SN
 974 energies. Here, we split the sample of Type IIn SNe into
 975 bright and faint subsamples to test whether they have simi-
 976 lar precursor rates. We consider a SN bright if it reaches an

977 absolute magnitude of -18.5 in any ZTF band. This thresh-
 978 old is chosen such that the measured precursor rates are rel-
 979 atively well constrained in both subsamples. Detections in
 980 all three bands are considered, because some SN light curves
 981 only have sparse observations, especially if their peak oc-
 982 curred in the year 2020, for which part of the data has not yet
 983 been released (see Sec. 2.2).

984 We compare the r -band precursor rates for bright and faint
 985 SNe in Fig. 9 and the subsample of bright SNe has a higher
 986 rate of bright precursors. The rate of faint precursors is not
 987 well constrained for the bright SN sample, because most ob-
 988 jects in this subsample are located at large distances. The
 989 rates could therefore agree below and absolute magnitude of
 990 -14 (see also Table 5). The difference between the bright
 991 and faint sample is relatively strong in the left-hand panel of
 992 Fig. 9, which shows the rate as the fraction of time during
 993 which the progenitor stars undergo precursors and thus de-
 994 pends on the precursor duration (see also Sec. 4.1). In the
 995 right-hand panel of the figure, we show instead the fraction
 996 of SNe that undergo a long-lasting precursor immediately be-
 997 fore the explosion (like in Fig. 8) and the difference is not
 998 significant any more. A possible explanation for this change
 999 could be that bright precursors have longer durations. In-
 1000 deed, the three brightest precursors in Fig. 5 are all observed
 1001 for ~ 100 days. We hence find indications that luminous
 1002 SNe typically undergo brighter and longer-lasting precursors.
 1003 This correlation is quantified in Sec. 5.2.

1004 4.4. Precursor Rates for Different Interacting SNe

1005 As described in Sec. 2.1, our full sample also contains in-
 1006 teracting SNe that do not belong to the class of Type IIn SNe.
 1007 Here, we present precursor rates for SNe of Type Ibn (based
 1008 on 12 objects for which pre-explosion observations are avail-
 1009 able; see the online version of Table 1), SLSNe-II (26 ob-
 1010 jects after excluding SN 2019meh which falls on top of a
 1011 background AGN), flash-spectroscopy SNe (20 objects), and
 1012 Type Ia-CSM SNe (7 objects). The number given in Table 5
 1013 can be lower as not all SNe have pre-explosion data in the r -
 1014 band. Flash-spectroscopy events are here defined as objects
 1015 showing narrow He II lines in their early-time spectra up to
 1016 a week after the discovery. There is some overlap between
 1017 flash-spectroscopy SNe and the other classes: Some flash-
 1018 spectroscopy SNe show narrow hydrogen lines for several
 1019 weeks and are here included in the sample of Type IIn SNe
 1020 (such as SN 2019cmy). SN 2019uo, is considered a Type Ibn
 1021 SN, even though it might show flash-spectroscopy lines at
 1022 early times (Gangopadhyay et al. 2020).

1023 We calculate the fraction of time during which precursors
 1024 are observed in the same way as in Sec. 4.1 and show the
 1025 results for each subsample in Fig. 10 for 7-day bins. The pre-
 1026 cursor detected prior to the Type Ibn SN 2019uo (described
 1027 in more detail in Sec. 5.3), does not appear because it is

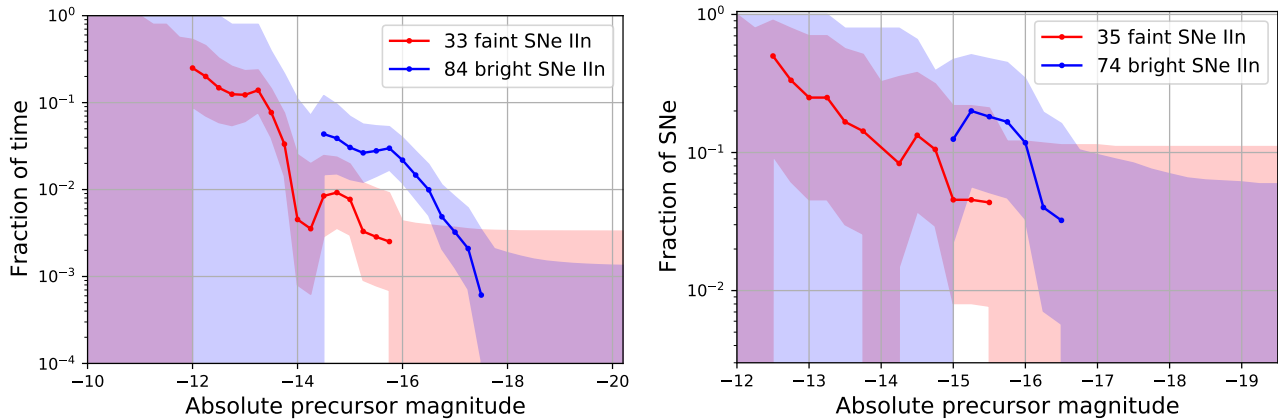


Figure 9. r -band precursor rates for faint and bright (peak magnitude < -18.5 in the g , r , or i band) SNe of Type II. The left plot displays the fraction of light-curve bins in which precursors are detected, which means that the rate depends on the precursor duration (like Fig. 7). The right figure is only based on well-observed SNe and the rate indicates whether a long-lasting precursor is detected within the last three months before the explosion (like in Fig. 8).

marginally above the 5σ threshold. An unconfirmed precursor is detected 680 days before the explosion of the Type Ia-CSM SN 2019yzx, as shown in Fig. 4. However, its significance is purely driven by observations in a single night while the two neighboring data points are consistent with zero. The location is observed relatively sparsely, so we cannot confirm whether the detection is real. We here conservatively assume that the detection is not astrophysical.

For comparison, the measured r -band precursor rate for Type II SNe (from the main panel of Fig 7) is shown as a dashed red line in Fig. 10. The Type II rate is nearly always in the allowed region of parameter space, which means that we do not expect to detect any precursors even if the rates are as high as for Type II SNe. The lower sensitivity is due to the small sample size, or in the case of SLSNe to the fact that the objects are located at large distances (see also Table 5). The only region where the Type II SN rate is higher than the upper limit is for the sample of flash-spectroscopy SNe at faint precursor magnitudes of > -14 . However, in this region the Type II SN rate is completely dominated by SN 2019fmb and we therefore consider it less reliable.

Thus, we conclude that we only observe a single precursor that was not associated with a Type II SN, but with the Type Ib SN 2019uo. However, this small number of detections is expected owing to the small sample sizes of the subclasses and to the large distances of SLSNe.

5. IMPACT OF THE PRECURSORS ON THE SNE

In this section we explore the impact of the observed precursors on the SN spectra and light curves. In Sec. 5.1 we find that the narrow emission lines in the spectra of most Type II SNe cannot originate from the material ejected during the observed precursors, but are instead produced by more distant material. Next, in Sec. 5.2 we test whether SNe with observed precursors are brighter than other SNe in our sample.

Finally, in Sec. 5.3 we describe how the precursor prior to the Type Ib SN 2019uo could account for both the SN light curve and the spectral evolution of this object.

5.1. Progenitor Mass-Loss History

A massive star of $100 M_{\odot}$ reaches its Eddington luminosity when it becomes brighter than 1.3×10^{40} ergs s^{-1} . For a hot LBV star with a temperature of 20,000 K (see, e.g., Smith et al. 2004) this luminosity corresponds of an absolute r -band magnitude of -8.1 , while it is -10.0 for a temperature of 5,000 K which is more similar to the temperatures observed for the precursors in Fig. 6. Figure 5 shows that the luminosities of all detected precursors are clearly above this threshold, so the outbursts are likely accompanied by strong mass-loss events.

By detecting the precursor, we measure the time of the mass ejection; however, the velocity of the material is uncertain (see also Sec. 6.1.2). The gray regions in Fig. 11 indicate out to which radii the material has expanded at the time of the SN explosion, depending on its velocity. CSM velocities between 0 and $1,500 \text{ km s}^{-1}$ are shown on the linear ordinate axis. We here assume that the material was ejected from a radius of $100 R_{\odot}$, 7×10^{12} cm. Using a radius that is a factor of a few larger or smaller does not have a major impact on the results, as spectra are usually obtained after the SN ejecta have expanded far beyond this radius.

Most detected precursors occur within the last few months before the explosion, so any ejected material is still located within a radius of 10^{15} cm even if it has a velocity of $\lesssim 1,000 \text{ km s}^{-1}$. Earlier precursors are only observed for six SNe (SN 2018eru, SN 2019uo, SN 2019bxq, SN 2019mom, SN 2020iq, and SN 2019edh; see Figs. 3, 4, and 5). The material ejected in these precursors might be located at radii of a few $\times 10^{15}$ cm, but likely below 10^{16} cm.

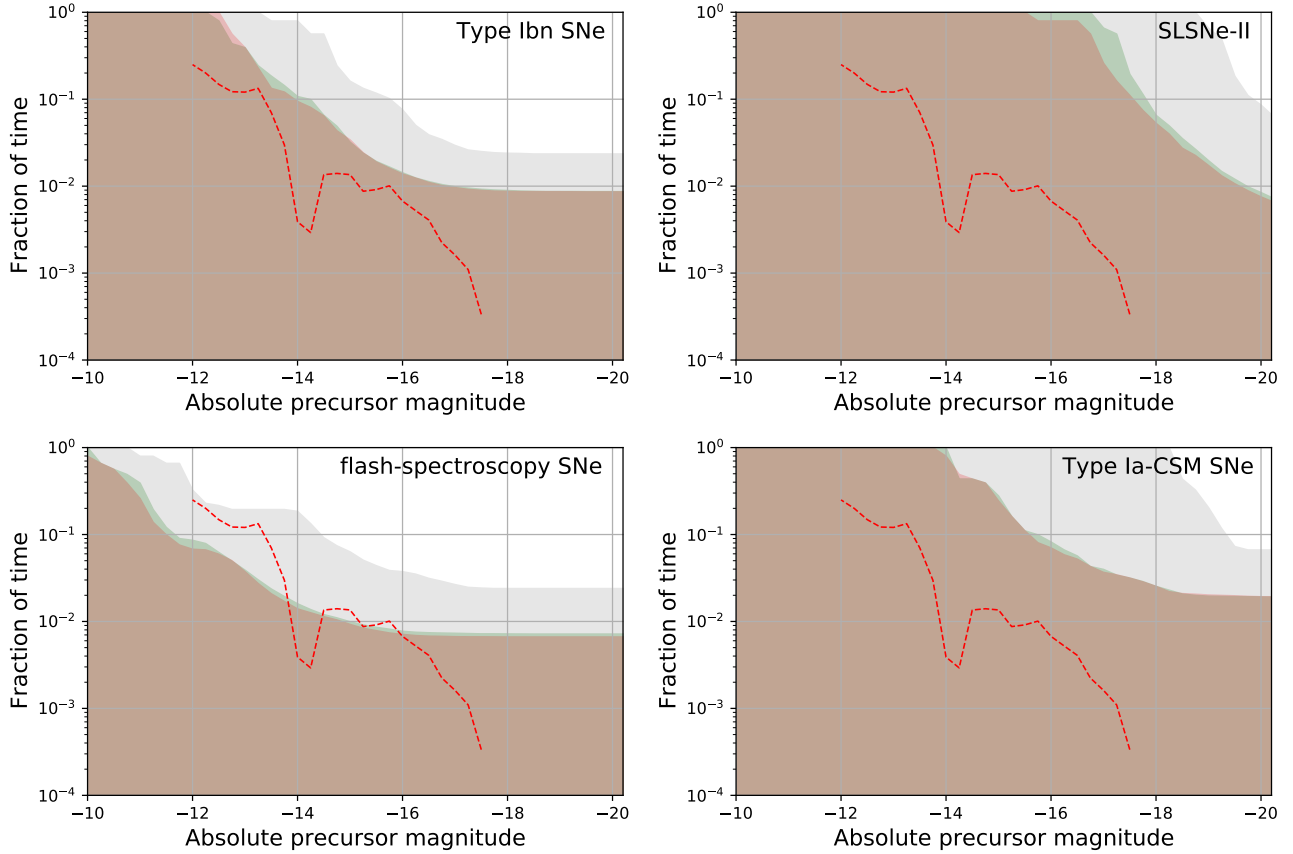


Figure 10. 95% upper limits on the precursor rates for 7-day bins for Type Ibn SNe, SLSNe-II, flash-spectroscopy events, and Type Ia-CSM SNe. The shaded areas indicate the 95% confidence area and the area above it excluded by the nondetection of precursors. The red dashed line indicates the r -band rate that was measured for Type IIc SNe in the main panel of Fig. 7.

1095 Next, we consider the narrow emission lines in the spectra of the SNe. To estimate CSM velocities, we measure the
 1096 full width at half-maximum intensity (FWHM) of the narrow
 1097 component of the $H\alpha$ line. We subtract the approximate resolution of the spectrograph in quadrature or quote upper limits
 1098 if the result is smaller than half of the resolution. In addition,
 1099 we look for narrow P Cygni features in the $H\alpha$ line (He lines
 1100 for the Type Ibn SN 2019uo), as their minimum indicates the
 1101 typical velocity of material moving toward the observer. The
 1102 results for all spectra with clear narrow features are listed in
 1103 Table 6. The quoted velocities are only order-of-magnitude
 1104 estimates as we do not fit line profiles, measure the actual res-
 1105 olution of the spectra, or subtract host-galaxy contributions.

1106 The exact location of the material that produces the narrow
 1107 features is unknown, but the time when the spectrum was
 1108 obtained provides an order-of-magnitude lower limit on its
 1109 radius. Narrow features can only originate from unshocked
 1110 material, which must be located at larger radii than the SN
 1111 ejecta. In order to estimate these radii, we adopt a fiducial
 1112 average ejecta velocity of 10^4 km s^{-1} , which is close to the
 1113 width of the broad hydrogen features observed in the late-
 1114 time spectra of SN 2018kag, SN 2019cmy, and SN 2019zrk.
 1115
 1116

1117 To estimate out to which radius the ejecta have approximately
 1118 expanded we multiply this velocity by the time since the ex-
 1119 plosion. The resulting distances and CSM velocities are repre-
 1120 sented by the data in Fig. 11, where blue points indicate
 1121 velocities measured from the line width while orange points
 1122 indicate the velocities of narrow P Cygni profiles. We em-
 1123 phasize that both the radii and velocities are rough estimates.

1124 For most SNe, the data points are located below or to the
 1125 right of the gray shaded region which indicates the location
 1126 of the CSM produced during the observed precursor. This
 1127 implies that the material ejected during the precursor can-
 1128 not account for the observed narrow emission lines, because
 1129 it would be located smaller radii if it propagates with the
 1130 observed velocity. Instead, it is more likely that the emis-
 1131 sion lines are produced by slow-moving material that was
 1132 expelled earlier. This conclusion is exclusively based on the
 1133 distance out to which the SN ejecta have expanded at a cer-
 1134 tain time and is therefore also valid for aspherical CSM dis-
 1135 tributions (see, e.g., Soumagnac et al. 2020), as long as the SN
 1136 ejecta expand with an average velocity of at least 10^4 km s^{-1}
 1137 in all directions. The only SNe for which the narrow fea-
 1138 tures might originate from CSM produced during the precu-

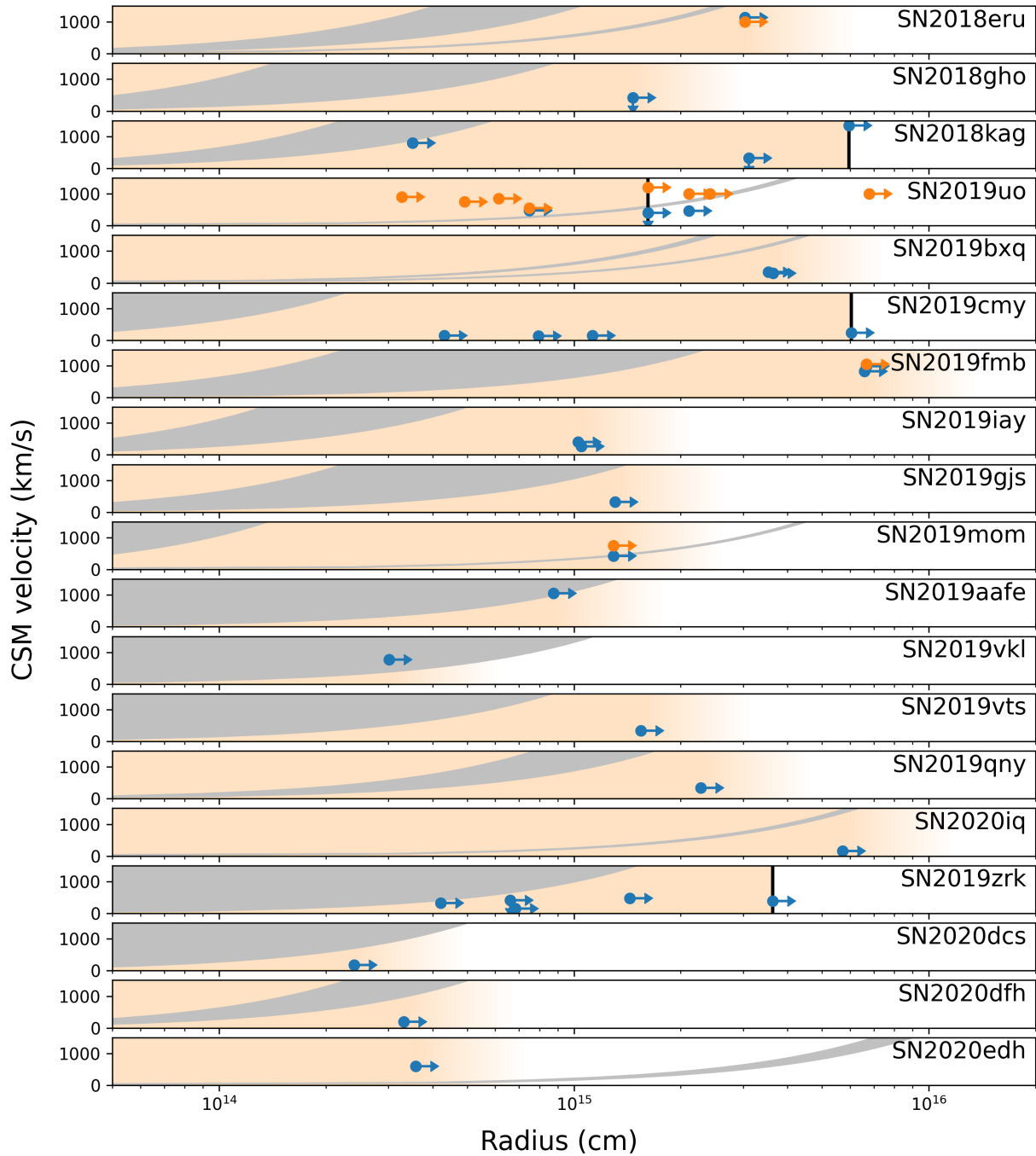


Figure 11. Radial CSM distribution for SNe with precursors. The gray regions indicate the possible locations of material ejected during the observed precursors depending on its velocity (shown on a linear scale). Data points correspond to spectra in which we observe narrow lines (blue points) or narrow P Cygni profiles (orange points). The ordinate represents the measured velocity while the abscissa is a lower limit on the radius of the material. The unshocked material must be located above the ejecta for which we assume a fiducial mean velocity of 10^4 km s^{-1} . For four SNe, black lines indicate that broad features from shocked material or the SN ejecta emerge, which means that the unshocked CSM is no longer optically thick. All other SNe are still optically thick at the time when the last spectrum is obtained and the shaded area represents a lower limit on the extension of the CSM.

1139 sor are SN 2019uo, SN 2019mom (material from the early
 1140 precursor), SN 2019aafe, SN 2019vkl, and SN 2020edh. In
 1141 all other cases, material ejected during the precursor is swept
 1142 up quickly if it has a low velocity or, if it is faster, it cannot
 1143 account for the low line velocities.

1144 The measured CSM velocities and the lower limits on the
 1145 radius allow us to roughly estimate when the material that
 1146 produces the narrow lines was ejected. In half of the spectra
 1147 we see matter that was presumably ejected at least 1 yr
 1148 before the explosion, while 10% of the spectra show signatures
 1149 of material ejected 2.5 yr or more before the SN. Additional
 1150 material could be ejected earlier and the resulting
 1151 CSM shells at larger distances can lead to rebrightenings
 1152 or bumps in the SN light curve, as observed for example
 1153 in SN 2009ip (Margutti et al. 2013), PTF 10tel (Ofek et al.
 1154 2013b), or iPTF 13z (Nyholm et al. 2017).

1155 We typically observe similar line velocities in spectra of
 1156 the same SNe, perhaps with the exceptions of SN 2018kag
 1157 and SN 2019uo, where the scatter is larger. One explanation
 1158 is that the narrow lines are produced by the same material that
 1159 is located at a large radius above the photosphere. Another
 1160 option is that progenitor stars eject material with a character-
 1161 istic velocity (see, e.g., Owocki et al. 2019, who find an
 1162 equipartition between the gravitational and kinetic energy of
 1163 material ejected from the surface of an LBV). If the CSM
 1164 velocities are indeed determined by the surface gravity of
 1165 the progenitor stars, the escape velocity of the progenitor
 1166 of SN 2019cmy (and maybe SN 2020dcs and SN 2020dfh,
 1167 for which we only have lower resolution spectra) are relatively
 1168 low as shown in Table 6. The escape velocity is determined
 1169 by the stellar mass and radius, and is given by
 1170 $v_{\text{escape}} = (2 \times G \times M/R)^{0.5}$. For a stellar mass of $30 M_{\odot}$,
 1171 the stars would have large radii of 300 to 500 R_{\odot} . The highest
 1172 escape velocities are observed for SN 2019uo, SN 2019fmb,
 1173 and SN 2019aafe, which would yield radii of only 10 R_{\odot} to
 1174 15 R_{\odot} , again assuming a stellar mass of $30 M_{\odot}$. Especially for
 1175 the Type Ibn SN 2019uo, this interpretation seems appropriate:
 1176 the star has already stripped its hydrogen envelope and is
 1177 therefore likely much more compact than a typical LBV star.

1178 For four SNe, broad emission lines or broad P Cygni features
 1179 become visible a few weeks or months after the SN
 1180 explosion. This suggests that the ejecta have reached the radius
 1181 where the CSM is optically thin. The corresponding radii are
 1182 marked by black lines for SN 2019uo, SN 2019cmy, SN 2019aafe,
 1183 and SN 2019zrk. The late-time spectra of the first three SNe
 1184 continue to exhibit narrow features on top of the broad line,
 1185 indicating that unshocked, optically thin material is still
 1186 located above the ejecta. Spectroscopic monitoring of SN
 1187 2019zrk continued and about one month after the broad features
 1188 first emerged, it turned into a Type II SN without any narrow
 1189 components (as will be described by Fransson et al., in prep.).
 1190 For all other SNe, the CSM is still optically

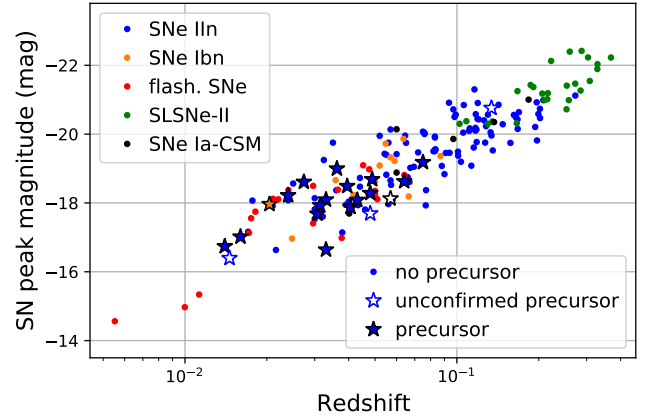


Figure 12. SN peak magnitudes for SNe with and without precursors. We use the brightest detection in the g , r , or i band as a proxy for the peak magnitude. The apparent correlation between the redshift and peak magnitude is caused by the Malmquist bias (Malmquist 1922). Most precursors are observed for relatively nearby SNe as they are faint. We find that SNe with detected precursors are not significantly more luminous than the complete sample. We do not apply K corrections as most precursors are detected for relatively nearby SNe.

1191 thick at the time when the last spectrum was obtained, mean-
 1192 ing that the dense CSM extends to larger radii as indicated by
 1193 the shaded area.

1194 We conclude that the material ejected during the observed
 1195 precursors typically cannot account for the narrow emission
 1196 lines in the SN spectra (see also Moriya et al. 2014). The narrow
 1197 lines that are observed while the SN is bright are instead
 1198 produced by slow-moving material ejected years before the
 1199 observed precursors and SN explosion.

1200 5.2. Correlations with SN Properties

1201 Here, we test whether the observed precursors increase the
 1202 SN peak brightness or prolong the rise time. Ofek et al.
 1203 (2014a) found several marginally significant and weak correla-
 1204 tions between the CSM mass estimate and the SN peak lumi-
 1205 nosity, rise time, and SN energy. All of these correlations
 1206 are based on a small sample of precursors and require confir-
 1207 mation. Figure 12 shows all SNe with and without precursors
 1208 and their peak magnitudes. Precursors are detected for many
 1209 nearby, faint Type IIn SNe, but not for nearby SNe of other
 1210 types with the exception of the Type Ibn SN 2019uo. Bright
 1211 precursors are rare, as demonstrated in Sec. 4, so fewer pre-
 1212 cursors are detected for distant SNe. The correlation between
 1213 the redshift and the SN luminosity in Fig. 12 is due to the
 1214 Malmquist bias (Malmquist 1922), which describes that faint
 1215 objects are undetectable at large distances.

1216 To quantify whether SNe with precursors of any luminosity
 1217 tend to be more luminous, we calculate a partial correlation
 1218 between the SN peak magnitude and an array which specifies
 1219 whether or not a precursor is detected. The distance modu-

lus is used as a control variable to correct for the impact of the Malmquist bias. The distance modulus is chosen rather than the redshift or distance, because it is proportional to the apparent SN magnitude and hence to the detection probability. The partial correlation is calculated for 116 Type II_n SNe with *r*-band pre-explosion observations and with measured peak magnitudes, and we find a Pearson correlation coefficient of 0.06 which corresponds to a *p*-value of 0.53. We thus do not detect a correlation between the SN peak magnitude and the detection of a precursor in our search. This might indicate that both groups of SNe have massive CSM shells.

In Sec. 4.3 we found indications that luminous SNe tend to have more luminous precursors (see Fig. 9). To quantify the significance of this observation we calculate a partial correlation between the precursor and the SN peak luminosity while again using the distance modulus as a control variable. The calculation is done for the *r*-band precursor magnitudes of 12 SNe that have long-lasting precursors in the final three months before the SN explosion, the same objects that contribute to the rate measurement in the right-hand panel of Fig. 9. We calculate the Spearman rank coefficient, which measures whether brighter precursors are associated with brighter SNe without assuming a linear relation between the two luminosities. We find a positive correlation with a correlation coefficient of 0.84 and a *p*-value of 0.001 or a significance of 3.1σ . We can hence confirm that more luminous precursors occur prior to more luminous SNe even after correcting for the impact of the Malmquist bias. There could be many possible explanations for the detected correlation: A more massive CSM might boost both the luminosity of the precursor and of the SN, or an energetic precursor could create a more massive CSM shell which results in stronger interaction and a more luminous SN (see also the simple exploration by Ofek et al. 2014a). Alternatively, stars with certain properties might produce more violent precursors and more energetic SN explosions. We also caution that less luminous SNe tend to be nearby while more luminous SNe are located at larger redshifts. While we corrected for the fact that distant SNe appear fainter on Earth, there could be many other differences between these objects which all might play a role.

A massive, optically thick CSM slows down the rise of the SN light curve because the photons diffuse out to the photosphere, and we thus expect a correlation between the SN rise time and the estimated precursor mass. To estimate the diffusion time we inspect the SN light curves in 1-day bins and quantify how many days it takes the light curve to reach its peak from a flux level that is 1.086 mag lower, which corresponds to a luminosity increase by a factor of *e*. This is done in the *r* band if available and in the *g* band for SN 2018gho. The *g* band typically peaks earlier than the *r* band, so the numbers might not be directly comparable. The rise time

should be measured for the bolometric light curve, which typically rises more quickly as a large part of the energy is emitted in the UV. Our estimates are hence upper limits on the actual rise time. The estimated rise times are given in the penultimate column in Table 4, if the rise and peak are well observed.

With rise times of 4–25 days, all SNe with detected precursors are part of the fast rising subgroup identified by Nyholm et al. (2020)⁶ which includes approximately two thirds of the Type II_n SNe in their sample. A likely explanation is that fast rising SNe II_n are typically fainter (Nyholm et al. 2020) and our precursor search is most sensitive to nearby, faint SNe (see Fig. 12). We here assume that energetic precursors eject more material and search for a correlation between the radiative precursor energy and the estimated SN rise time. With a Pearson correlation coefficient -0.37 with a *p*-value of 0.25, no significant correlation is found. It is either possible that a relation is washed out owing to the large uncertainties on both quantities or the observed precursors do not dominate the total CSM mass.

In conclusion, we do observe that more luminous precursors are detected prior to more luminous SNe even after correcting for the impact of the SN distance. However, SNe with detected precursors are not systematically more luminous than SNe without detected precursors, and we do not measure a correlation between the precursor energy and the SN rise time. Thus, we do not find that the observed precursors have a major impact on the SN light curve. This seems to fit with our results from Sec. 5.1, where we find that the narrow hydrogen features in the spectra of Type II_n SNe typically do not originate from material ejected during the observed precursor. Together, both results might indicate that a large fraction of the CSM is ejected in earlier mass-loss events that we do not detect here.

5.3. The Type Ib_n SN 2019uo

One of the precursors discovered in this study occurs prior to SN 2019uo, making it the second Type Ib_n with a detected precursor after SN 2006jc (Pastorello et al. 2007; Foley et al. 2007). The coadded difference images in Appendix A confirm that a point source is visible ~ 320 days before the explosion of SN 2019uo. As shown in Fig. 13, the precursor starts ~ 340 days before the explosion of SN 2019uo and is observed over 35 days (see also Fig. 3 and Table 4). In addition to the 5σ detection, another two data points surpass the 3σ threshold when using 7-day bins, and in total 24 individual images contribute to the detection. The mean precursor

⁶ While we define the rise time as the time it takes the SN to rise by a factor of *e* to its peak, Nyholm et al. (2020) determine the rise time from a power-law fit. Thus, the quoted numbers might not be directly comparable, but the bottom panel of their Fig. 7 allows us to read off rise times that are consistent with our definition.

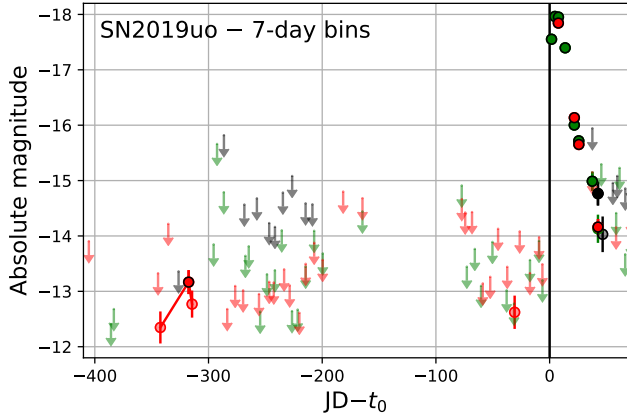


Figure 13. Light curve of SN 2019uo in 7-day bins before the estimated explosion date (JD 2,458,501.3) and in 1-day bins afterward. Solid data points with black edges are 5σ detections, transparently colored data points have significances larger than 3σ , and upper limits are less significant. Green, red, and black data points correspond to observations in the g , r , and i bands, respectively. The 3σ detection at ~ 30 days could be a statistical fluctuation and is not discussed here.

magnitude is -13 , making it one of the faintest precursors detected in this search. The observed radiative energy in the r band is 1.7×10^{47} ergs s^{-1} . However, the observations shortly before and after the precursor are not very constraining, so it could last longer.

With a redshift of 0.020, SN 2019uo is the closest Type Ibn SN out of the 12 objects in our sample. It was classified as a Type Ibn based on a spectrum showing narrow helium P Cygni features that was obtained 9 days after the estimated explosion date (Fremling et al. 2019). SN 2019uo was studied by Gangopadhyay et al. (2020) in detail, and they find that SN 2019uo is slightly underluminous and evolves quickly, typical for Type Ibn SNe. They model the bolometric light curve with CSM interaction and their best-fitting models require the presence of $0.4\text{--}0.7 M_{\odot}$ of material located at a radius of $\gtrsim (0.2\text{--}2) \times 10^{15}$ cm.

SN 2019uo is one of the few objects for which the narrow P Cygni profiles in the spectra might originate from the CSM ejected during the observed precursor (see Fig. 11). We measure typical velocities of ~ 900 km s^{-1} (see Table 6), which would imply that the CSM has propagated to a radius of a $\sim 2 \times 10^{15}$ cm when the SN explodes 320 days after the precursor. This radius is approximately consistent with the inner CSM radius required by the modelling of Gangopadhyay et al. (2020). Moreover, it roughly coincides with the radius at which the CSM turns optically thin shown in Fig. 11: broad features, likely from the shocked CSM, first appear in a spectrum obtained 18 days after the explosion date (see Fig. 3 by Gangopadhyay et al. 2020). A CSM shell located at a radius of 2×10^{15} cm is swept up by the SN ejecta if they have an average velocity of $13,000$ km s^{-1} . Narrow helium fea-

tures remain visible in later spectra and might originate from an optically thin wind located above the CSM. The same material could also produce the flash-ionization features detected by Gangopadhyay et al. (2020) before the SN reaches its peak.

The observed precursor energy can be produced via interaction if the mass lost during the precursor is $\gtrsim 0.007 M_{\odot}$ (see Fig. 14 or Table 4). However, the SN light curve modelled by Gangopadhyay et al. (2020) requires a CSM mass a factor of 50–100 times larger. A possible explanation is that the material ejected during the precursor propagates through a low-density environment such that only 1–2% of its kinetic energy is converted to radiation in the r band. This would imply that the progenitor star was not surrounded by a massive CSM before the observed precursor. Alternatively, only a small fraction of the CSM is emitted during the observed precursor and the rest of the required material is expelled during earlier or fainter precursors which we do not detect. In this case the radiative efficiency would be larger. We conclude that a relatively simple picture can explain the characteristics of the precursor and subsequent SN: the observed precursor could produce the complete CSM of $\sim 0.5 M_{\odot}$ if its radiative efficiency is low with $\epsilon \approx 1\%$. The resulting dense CSM shell is confined to a radius of $\sim 2 \times 10^{15}$ cm and can account for the SN bolometric light curve (shown by Gangopadhyay et al. 2020) as well as for the spectroscopic development.

Until now, the only precursor observed prior to a Type Ibn SN was observed for SN 2006jc (Pastorello et al. 2007; Foley et al. 2007). The 9-day-long precursor with a peak magnitude of -14.1 was detected 2 yr before the SN explosion. The two precursors are hence similar to each other, as they are both relatively faint and happen hundreds of days before the SN explosion. In both cases, the CSM is helium-rich, so we do not witness the stripping of the hydrogen envelope which happened only decades to centuries prior to the explosion of the Type Ib SN 2014C (Margutti et al. 2017). Based on 11 Type Ibn SNe with pre-explosion data in the r band, we show in Fig. 10 and Table 4 that precursors with an r -band magnitude of < -16 happen $< 1.4\%$ of the time (95% confidence level), while faint precursors with magnitudes brighter than -13 might happen up to 38% of the time. These limits are based on observations collected up to 2.5 yr before the SN explosion and the median observation time is 8.6 months before the explosion. We thus do not have very strong constraints on faint outbursts and they might be relatively common.

Thus, we confirm that the progenitor stars of some Type Ibn SNe are able to produce relatively bright flares in the last years before their explosion. Except for the two precursor detections, no Type Ibn SN progenitor has been identified in archival observations and their nature is debated. The most commonly suggested progenitors are Wolf-Rayet stars that

1401 have shed their hydrogen envelopes or massive stars that are
 1402 stripped by a binary partner (see, e.g., [Smith 2017](#); [Hossein-](#)
 1403 [zadeh et al. 2017](#)). Alternatively, the progenitors of some
 1404 Type Ibn SNe were hypothesized to be white dwarf bina-
 1405 raries ([Sanders et al. 2013](#); [Hossein-zadeh et al. 2019](#)), or very
 1406 massive stars that undergo pulsational pair instability events
 1407 ([Woosley 2017](#); [Karamehmetoglu et al. 2019](#)) which would
 1408 imply that no core collapse occurs and the star is likely still
 1409 present. Contrary to LBVs, classical Wolf-Rayet stars are not
 1410 known to undergo giant eruptions, so bright flares cannot be
 1411 common during the lifetime of the star. There is an inter-
 1412 mediate class of Ofpe/WN9 stars which have stripped most
 1413 of their hydrogen envelope, but undergo LBV-like outbursts
 1414 (see, e.g., [Smith et al. 2020](#)). Such stars have been suggested
 1415 as progenitors for two Type Ibn SNe that also show rela-
 1416 tively strong hydrogen lines ([Smith et al. 2012](#); [Kool et al.](#)
 1417 [2020](#)). However, the hydrogen features in the spectra of
 1418 SN 2006jc are much weaker and SN 2019uo might not show
 1419 any hydrogen. It is therefore unclear under which conditions
 1420 stripped-envelope stars can produce as bright eruptions. If
 1421 such flares are related to the late stages of nuclear burning
 1422 (see [Sec. 6.2](#)), they would only occur shortly before the SN
 1423 explosion, which would explain why no such flares are ob-
 1424 served for Wolf-Rayet stars in the Milky Way or in nearby
 1425 galaxies.

1426 6. NATURE OF THE PRECURSORS

1427 We emphasize that the nature of the observed transients is
 1428 ambiguous. Owing to the optically thick CSM, we cannot
 1429 directly observe the expanding SN ejecta, but only see light
 1430 diffusing out through the photosphere. We therefore cannot
 1431 determine whether core collapse occurred or at what time
 1432 it happened (see, e.g., [Moriya 2015](#); [Tartaglia et al. 2016](#);
 1433 [Woosley 2017](#) for possible scenarios). It is conceivable that
 1434 some of the precursors are already part of the SN light curve,
 1435 rather than preceding the explosion. Nevertheless, in the
 1436 following we adopt the interpretation that core collapse oc-
 1437 curs shortly before the SN rises to its main peak and that the
 1438 precursors are produced by the progenitor star before it ex-
 1439 plodes.

1440 In [Sec. 6.1](#) we explore whether the precursor luminosity
 1441 could be produced via interaction or by a continuum wind.
 1442 The underlying energy source is unknown and suggested
 1443 mechanisms include unstable nuclear burning phases ([Smith](#)
 1444 [& Arnett 2014](#)), shell burning ([Arnett & Meakin 2011a,b](#)),
 1445 interaction with a binary companion ([Smith & Arnett 2014](#);
 1446 [Mcley & Soker 2014](#); [Danieli & Soker 2019](#); [Owocki et al.](#)
 1447 [2019](#)), or reduced gravity due to high neutrino luminosities
 1448 ([Moriya 2014](#)). Specific predictions exist for wave-driven
 1449 mass loss triggered by instabilities during the neon and oxy-
 1450 gen burning phases, and we compare our observations to the
 1451 model described by [Shiode & Quataert \(2014\)](#) in [Sec. 6.2](#).

1452 6.1. What Powers the Precursor Luminosity?

1453 In this section we explore possible mechanisms that could
 1454 produce the observed precursor luminosity. First, we point
 1455 out in [Sec. 6.1.1](#) that the long precursor durations likely re-
 1456 quire a persistent energy source. This could, for example, be
 1457 interaction of the ejected material with pre-existing CSM (de-
 1458 scribed in [Sec. 6.1.2](#)) or a brightening of the star (discussed
 1459 in [Sec. 6.1.3](#)). We show that interaction-powered precu-
 1460 rsors require extensive mass loss of up a solar mass, while
 1461 a continuum-driven wind would result in a ~ 10 times lower
 1462 mass loss. The two scenarios could hence be distinguished
 1463 by measuring the CSM masses, and we provide rough esti-
 1464 mates of the total mass in [Sec. 6.1.4](#).

1465 6.1.1. Precursor Durations

1466 The densely sampled light curves of the ZTF survey allow
 1467 us to measure the durations for a sample of precursors. As
 1468 shown in [Fig. 5](#), the outbursts are typically observed over sev-
 1469 eral months. Their true durations are likely even longer, if the
 1470 fainter parts of the precursors remain undetected. With rise
 1471 times of only ~ 1 mag over ~ 50 – 100 days, most precursors
 1472 develop much more slowly than the subsequent SNe. This
 1473 implies that the diffusion time in the CSM does not domi-
 1474 nate the precursor duration. Consequently, the precursors are
 1475 likely not powered by a single short-lived eruption from the
 1476 stellar surface, but require a long-lived energy source, such as
 1477 ongoing interaction, a stellar wind, potentially a series of ex-
 1478 plosions, or maybe a short-lived event deep within the stellar
 1479 envelope, where the diffusion time is much larger than within
 1480 the CSM. We thus conclude that the long duration of several
 1481 detected precursors is likely intrinsic and not due to diffusion.

1482 6.1.2. Interaction-Powered Precursors

1483 The light curves of Type IIIn SNe are mainly powered by
 1484 interaction between the ejecta and the circumstellar material
 1485 surrounding the star. It thus might seem logical that the same
 1486 is true for the precursors. In this scenario, a large amount of
 1487 material is ejected from the stellar surface and a fraction of
 1488 the kinetic energy $\epsilon < 1$ is converted to radiative energy when
 1489 the ejected material is slowed down by pre-existing CSM. If
 1490 the velocity of the newly ejected material is known, its mass
 1491 can be estimated using

$$1492 E_{\text{rad}} = \epsilon E_{\text{kin}} = \epsilon \frac{1}{2} M_{\text{CSM, pre.}} v_{\text{CSM, pre.}}^2, \quad (1)$$

1493 where $M_{\text{CSM, pre.}}$ and $v_{\text{CSM, pre.}}$ are respectively the mass and
 1494 velocity of the material ejected during the precursor.

1495 Equation 1 shows that the required CSM mass strongly
 1496 depends on the velocity. CSM velocities can be estimated
 1497 from the narrow hydrogen (or helium) features, however; as
 1498 demonstrated in [Sec. 5.1](#), these lines are likely produced by
 1499 material ejected at earlier times. It is hence possible that the

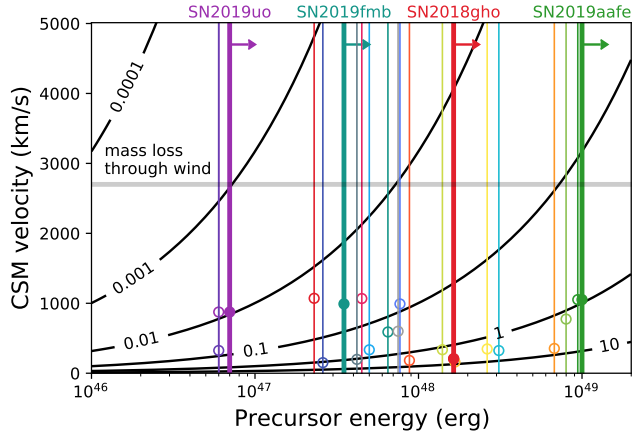


Figure 14. CSM masses required to produce the observed precursor energies, if they are powered by interaction. The black contour lines show the amount of CSM, $M_{\text{CSM, pre}}$, in solar masses, ejected during the precursor if the kinetic energy is completely converted to radiation (i.e., $\epsilon = 1$). The observed precursor energies (taken from Table 4) are indicated by vertical lines. They are lower limits on the actual radiative energy as we only detect the brightest part of the precursors and because we did not apply a bolometric correction when calculating the energy. CSM velocities measured from the spectra are marked by dots, but they do not necessarily correspond to the velocities of the precursor material. The gray horizontal line shows the approximate amount of CSM that a continuum-driven wind would eject (see Sec. 6.1.3).

1499 matter expelled during the observed precursors has larger ve-
 1500 locities which would result in lower CSM mass estimates.
 1501 The observed velocities and corresponding CSM masses are
 1502 given in the fourth and third to last columns of Table 4 (the
 1503 quoted velocity is the median of all spectra given in Table 6).
 1504 The required CSM masses for different velocities are illus-
 1505 trated in Fig. 14 for some of the precursors.

1506 Most observed precursors develop quite slowly as pointed
 1507 out in Sec. 6.1.1. Nyholm et al. (2020) measured the rise
 1508 and decline rates for ~ 30 Type II_n SNe from the PTF/iPTF
 1509 sample and the precursors we detect rise more slowly than
 1510 any Type II_n SNe in their sample. A possible explanation
 1511 could be that the precursor shock front propagates with a
 1512 substantially lower velocity compared to the SN ejecta. As a
 1513 consequence, the rate at which CSM is swept up is lower
 1514 and kinetic energy is converted to radiation more slowly.
 1515 According to the model by Svirski et al. (2012) (see also
 1516 Ofek et al. 2014b), the radiated luminosity produced during
 1517 CSM interaction is $L_{\text{pre}} \propto r^2 \rho v_{\text{CSM, pre}}^3$, which simplifies to
 1518 $L \propto v_{\text{CSM, pre}}^3$ for a wind-like density profile with $\rho \propto r^{-2}$.
 1519 The luminosity difference between precursors and SNe on
 1520 the order of 100 suggests that the average shock velocity is
 1521 a factor of ~ 5 lower (i.e., $v_{\text{CSM, pre}} \approx 2000 \text{ km s}^{-1}$
 1522 compared to $\sim 10^4$ for SN ejecta). However, this assumes that
 1523 the radiative efficiency ϵ (i.e., the fraction of kinetic energy

1524 that is converted to radiation) is similar for the precursor and
 1525 the SN. These higher velocities would reduce the amount of
 1526 ejected material by about one order of magnitude as shown
 1527 in Fig. 14.

1528 Interaction stops either when the shock reaches the edge of
 1529 the CSM or when it is slowed down, which happens when the
 1530 mass of the swept-up CSM is comparable to the mass in the
 1531 shock front. Several precursors (e.g., prior to SN 2019vkl,
 1532 SN 2019aafe, or SN 2019zrk) continue to rise for more than
 1533 100 days. If their luminosity is dominated by interaction,
 1534 the associated mass loss must be substantial, such that the
 1535 ejected material is not slowed down considerably within this
 1536 time (i.e., $\epsilon \ll 1$). If it expands with an average veloci-
 1537 ty of $2,000 \text{ km s}^{-1}$ it reaches a radius of $\sim 2 \times 10^{15} \text{ cm}$
 1538 within 100 days. Several other precursors (e.g., prior to
 1539 SN 2019fmb, SN 2019gjs, or SN 2020dcs) fade in the weeks
 1540 to months before the SN explosion, as was also observed for
 1541 the 2012a event prior to the final explosion of SN 2009ip.
 1542 This might indicate that the material has slowed down or that
 1543 it only collides with a thin CSM shell and then continues to
 1544 expand through a lower density environment. This qualitative
 1545 description assumes that each precursor is associated with a
 1546 single short-lived mass-loss event. It is, however, also possi-
 1547 ble that material is ejected in a series of eruptions from the
 1548 stellar surface. If the energy of these eruptions changes with
 1549 time, this could account for both rising or falling precursor
 1550 light curves.

1551 We conclude that the observed precursors could be pow-
 1552 ered by interaction if the star undergoes major mass-loss
 1553 events. The precursor luminosities require that the ejected
 1554 material has velocities on the order of $\sim 2,000 \text{ km s}^{-1}$. Such
 1555 low-velocity shock fronts could explain the long duration of
 1556 the precursors compared to the SN light curve. Figure 14
 1557 shows that the most energetic precursor requires the ejection
 1558 of $\sim 0.3 M_{\odot}$ of material for a CSM velocity of $2,000 \text{ km s}^{-1}$.
 1559 However, a more realistic radiative efficiency of $\epsilon \lesssim 0.3$
 1560 would bring the required mass back to $\sim 1 M_{\odot}$. CSM en-
 1561 velopes of several solar masses have been observed for some
 1562 Type II_n SNe, so high-mass estimates are not necessarily
 1563 unrealistic, and for less energetic precursors the required
 1564 masses are lower by a factor of up to 100.

1565 6.1.3. Wind-Driven Precursors

1566 In an alternative scenario the observed luminosity origi-
 1567 nates from the star itself. Shaviv (2001a) showed that the
 1568 outer part of the stellar envelope (from the radius out to which
 1569 convection is efficient to the “hydrostatic surface” of the star)
 1570 becomes unstable when the stellar luminosity approaches the
 1571 Eddington limit. Local density differences reduce the effec-
 1572 tive opacity of the star, so it remains quasistable even when
 1573 it exceeds the Eddington luminosity. However, the instabil-
 1574 ities only have an effect as long as the atmosphere is opti-

1575 cally thick over a scale height. An optically thick continuum-
 1576 driven wind is therefore accelerated from this region, with
 1577 the actual photosphere sitting farther out. The resulting mass
 1578 loss is smaller than can be expected without the lower ef-
 1579 fective opacity. The resulting wind has a typical velocity
 1580 of $(L/L_{\text{Eddington}})^{0.5} v_{\text{escape}}$ (Shaviv 2001b) — that is, usually
 1581 $v_{\text{CSM, pre.}} \gtrsim 1000 \text{ km s}^{-1}$, which is larger than most line ve-
 1582 locities measured in Sec. 5.1.

1583 Contrary to the interaction scenario a fraction of the radiative
 1584 energy is converted into kinetic energy (i.e., $\epsilon > 1$). The
 1585 mass loss can be calculated using

$$E_{\text{rad}} = \frac{1}{W} M_{\text{CSM, pre.}} c_s c = \epsilon E_{\text{kin.}} \quad , \quad (2)$$

1586 where $W \approx 5$ is an empirical factor, $c_s \approx 60 \text{ km s}^{-1}$ is the
 1587 speed of sound at the base of the optically thick wind (Shaviv
 1588 2000, 2001b), and c is the speed of light. We note that the
 1589 results of Eq. 2 are equal to Eq. 1 for a CSM velocity of
 1590 $v_{\text{CSM, pre.}} = 2,700 \text{ km s}^{-1}$ and $\epsilon = 1$. As a result the mass loss
 1591 is lower by a factor of ~ 10 compared to the numbers given
 1592 in the third to last column of Table 4. The most energetic
 1593 precursor with a radiative energy of 10^{49} ergs only results in
 1594 a mass loss of $0.1 M_{\odot}$ as shown in Fig. 14.

1595 Once the wind reaches an equilibrium state, it forms a pho-
 1596 tosphere. Owocki & Shaviv (2016) show that a wide range
 1597 of mass-loss rates and wind velocities result in photospheric
 1598 temperatures between 5,000 K and 6,000 K, the temperature
 1599 at which hydrogen recombines and the opacity drops. These
 1600 temperatures are consistent with most observed precursor
 1601 temperatures in Sec. 3.3. Larger temperatures are expected
 1602 before the wind reaches its equilibrium state, but lower tem-
 1603 peratures are more difficult to explain. We note that the pre-
 1604 cursor temperatures are also similar to the temperature of the
 1605 giant eruption of η Carina (Rest et al. 2012).

6.1.4. Constraints on the CSM Mass

1607 We also estimate upper limits on the total CSM mass (here
 1608 material located within 5×10^{15} cm) based on the SN rise
 1609 time. A massive, optically thick CSM slows down the rise
 1610 of the SN light curve, because the photons diffuse out to the
 1611 photosphere. Therefore, a quickly rising SN is inconsistent
 1612 with a large CSM mass, while a slow rise could be intrinsic
 1613 and does not necessarily imply a massive CSM. SN rise times
 1614 were estimated in Sec. 5.2 and are given in Table 4. For an
 1615 infinite wind-like CSM profile (i.e., with a density that de-
 1616 creases with the radius like $\rho \propto r^{-2}$), the diffusion time t_{diff} is
 1617 given by

$$t_{\text{diff.}} \approx \frac{\kappa K}{c} (\ln(c/v_{\text{shock}}) - 1) \quad , \quad (3)$$

1618 where κ is the opacity, v_{shock} is the velocity of the shock
 1619 front, and the mass-loading factor K is defined as $K =$
 1620 $\dot{M}/(4\pi v_{\text{CSM}})$ for the mass-loss rate \dot{M} and the CSM veloc-
 1621 ity v_{CSM} (Ginzburg & Balberg 2012).

1622 The CSM mass between two radii R_{inner} and R_{outer} can be
 1623 obtained by integrating the CSM density profile:

$$\begin{aligned}
 M_{\text{CSM, diff.}} &= \int_{R_{\text{inner}}}^{R_{\text{outer}}} 4\pi r^2 K r^{-2} dr = 4\pi K (R_{\text{outer}} - R_{\text{inner}}) \\
 &\approx 4\pi R_{\text{outer}} \frac{t_{\text{diff}} c}{\kappa (\ln(c/v_{\text{shock}}) - 1)} \\
 &\approx 0.10 R_{\text{outer, } 5e15 \text{ cm}} t_{\text{diff, 1d}} M_{\odot} \quad . \quad (4)
 \end{aligned}$$

1624 In the second line, we assume that the inner radius is much
 1625 smaller than the outer one and insert Eq. 3. We then adopt a
 1626 typical value for $\kappa = 0.34 \text{ cm}^2 \text{ g}^{-1}$, appropriate for a medium
 1627 that consists of 70% hydrogen (see, e.g., Ginzburg & Bal-
 1628 berg 2012; Ofek et al. 2013a) and a shock velocity of $v_{\text{shock}} =$
 1629 10^4 km s^{-1} . The CSM mass is hence proportional to the dif-
 1630 fusion time as well as to the outer radius of the CSM.

1631 We integrate the CSM density out to a radius of 5×10^{15} cm,
 1632 which is approximately consistent with the observed spectral
 1633 evolution shown in Fig. 11. The resulting upper limits on the
 1634 CSM masses are given in the last column of Table 4. While
 1635 many of the mass upper limits are consistent with the mass
 1636 estimates for interaction-powered precursors, there are dis-
 1637 crepancies for a few objects (e.g., SN 2019zrk, SN 2019gjs,
 1638 or SN 2018gho). We emphasize that a difference of a fac-
 1639 tor of a few does not necessarily imply an inconsistency, as
 1640 both CSM masses are order-of-magnitude estimates owing
 1641 to the assumed wind-like density profile, the adopted shock
 1642 velocity, and the outer CSM radius of 5×10^{15} cm. Further-
 1643 more, the diffusion time might be different for nonspherical
 1644 CSM geometries (Soumagnac et al. 2020). Another alterna-
 1645 tive would be considerably higher CSM velocities of a few
 1646 $\times 1,000 \text{ km s}^{-1}$ (see Sec. 6.1.2). We summarize that several
 1647 SNe, such as SN 2019zrk, rise quickly even though they ex-
 1648 perience powerful precursor eruptions shortly before the ex-
 1649 plosion. This might imply that the precursors are not associ-
 1650 ated with mass-loss events of several solar masses. Careful
 1651 modeling of a well-observed SN with an energetic precursor
 1652 would be required to establish whether fast SN rise times can
 1653 be reconciled with extensive mass-loss episodes in the last
 1654 months before the explosion.

6.2. Can Wave-Driven Mass Loss Trigger the Detected Precursors?

1655 Unbinding a solar mass of material requires a substantial
 1656 energy deposition in the stellar envelope. The fact that the
 1657 precursor rate increases in the last months before the SN ex-
 1658 plosion could imply that the precursors are associated with
 1659 late nuclear burning stages which last from a few years to a
 1660 few months (see, e.g., Shiode & Quataert 2014).

1661 When fusing carbon or heavier elements, both the energy
 1662 production and neutrino cooling rates increase dramatically
 1663 in the stellar core (see, e.g., Woosley et al. 2002; Arnett &
 1664 Meakin 2011a; Quataert & Shiode 2012). While the two pro-

cesses are in equilibrium on average, local imbalances cause vigorous convection within the core and Shiode & Quataert (2014) estimate that $\lesssim 10\%$ of the fusion energy is carried by convection. The convection excites gravity waves which typically remain confined to the core (Meakin & Arnett 2006; Quataert & Shiode 2012) and do not affect the envelopes of most massive stars. However, the internal structure of some progenitor stars may allow part of the wave energy to tunnel out of the core and excite acoustic waves in the stellar envelope. The energy deposited in the envelope can be as large as a few times 10^{40} ergs s^{-1} or $\sim 10^{47}$ ergs over a year. It might trigger strong adiabatic mass-loss events or inflate the stellar envelope Quataert & Shiode (2012); Shiode & Quataert (2014); Quataert et al. (2016); Fuller (2017).

The neon and oxygen burning phases last a few years to months with more massive cores burning out more quickly (see, e.g., Shiode & Quataert 2014). Silicon fusion only occurs in the last few days to hours before the explosion and therefore cannot account for the observed months-long precursors. Shiode & Quataert (2014) modelled different progenitor stars with the *MESA* stellar code (Paxton et al. 2011) and found that it takes the waves about several weeks to about a year to reach the stellar surface and that progenitor stars with a wide range of initial conditions can fulfill the requirements for matter outflow. We observe that the brightest precursors start several months before the SN explosion. They hence might be powered by energy produced during the neon or oxygen burning phases. According to the model by Shiode & Quataert (2014), the time of the precursor eruption is inversely related to the core mass. A precursor that occurs one month before the SN explosion would imply a helium core mass of $\lesssim 15 M_{\odot}$, while a precursor one year before the explosion requires a lower core mass of $\lesssim 5 M_{\odot}$.

The most energetic precursor, detected prior to the explosion of SN 2019aafe, released an *r*-band energy of 10^{49} ergs over 100 days. If this luminosity is interaction-powered, the kinetic energy would be even larger. For progenitors with $\sim 15 M_{\odot}$ helium cores, Shiode & Quataert (2014) calculate wave energies of up to a few times 10^{47} ergs, about 50 times lower than the observed radiative energy. Ten times higher energies could be reached by stars with $\gtrsim 30 M_{\odot}$ helium cores, but their oxygen burning phase only lasts for about a month, such that the produced waves only reach the surface days before the SN explosion. Fusing $\sim 1 M_{\odot}$ of material releases an energy of $\sim 10^{51}$ ergs during the neon and oxygen burning phases each (Quataert & Shiode 2012), so the wave transport would have to be extremely efficient to produce as energetic precursors as observed. The precursors observed prior to other SNe, such as SN 2019fmb or SN 2020dcs, are at least 10 times less energetic and are more easily explained by the model.

We summarize that wave-driven mass loss, powered by instabilities during the neon and oxygen burning phases, could explain why precursor eruptions occur in the last few months before the SN explosion. According to the model by Shiode & Quataert (2014), less energetic early precursors are produced by lower mass stars, while stars with massive cores produce more powerful precursors that occur only days before the explosion. This could at least qualitatively explain our observation that brighter precursors become more common in the last months before the SN explosion (see Sec. 4.2). However, the brightest detected precursor is about two orders of magnitude more energetic than predicted by Shiode & Quataert (2014), and it is unclear whether the model could account for such events. We emphasize that our observations cannot confirm that wave-driven mass loss triggers precursor eruptions, and that other mechanisms such as interaction with a binary companion star might also be able to explain the observations (see, e.g., Quataert et al. 2016; Owocki et al. 2019).

7. CONCLUSIONS

One main finding of this study is that bright precursors are relatively common immediately before the explosion of Type II_n SNe (see Fig. 5) and that most of them last for one or several months. Long-lasting precursors that are brighter than -13 mag in the *r* band are observed immediately prior to the explosion of about 25% of all Type II_n SNe (with a 95% confidence range of 5–69%). Some of the brightest precursors are better described as a continuous brightening rather than a discrete flare (see, e.g., the precursor light curves prior to SN 2019zrk or SN 2019aafe in Fig. 5). The most powerful precursor found here releases an energy of 10^{49} ergs over 100 days ($\sim 10\%$ of the radiative energy released in a typical SN explosion), but most precursors are an order of magnitude less energetic.

All precursors are much brighter than the Eddington luminosity of a massive star, such that they likely involve extensive mass-loss events. The mass of the ejected CSM is difficult to quantify: if the kinetic energy of the CSM is similar to the radiative energy of the precursor, the mass loss would typically amount to one or a few solar masses with large uncertainties owing to the unknown CSM velocity. For wind-driven precursors, the expected mass loss is typically ten times lower. Several SNe with detected precursors rise to their peak luminosity within a few days, which might imply that the mass of their CSM shell is typically $\lesssim 1 M_{\odot}$.

To our knowledge, such bright and long-lasting precursors have so far only been detected prior to Type II_n SNe and precursors prior to other SNe are typically less energetic. Nevertheless, material ejected during these events cannot account for the characteristic narrow hydrogen emission lines in the spectra of these SNe. Within the short time before the SN ex-

1769 plosion the ejected material cannot expand to radii larger than
 1770 10^{14} cm, if its velocity is as low as the line widths indicate.
 1771 Hydrogen emission lines are, on the other hand, observed for
 1772 many weeks or even years and are thus produced by material
 1773 located at larger radii. For the average spectrum, this material
 1774 must have been ejected at least ~ 1 yr before the explosion.
 1775 We only find few, rather faint and short, precursors at these
 1776 times. This might indicate that earlier mass-loss events are
 1777 likely substantially fainter than the observed precursors and
 1778 therefore remain undetected. SNe with precursors are not
 1779 significantly brighter than SNe without observed precursors
 1780 at similar redshifts, which likely supports our hypothesis that
 1781 the precursors detected immediately before the explosion do
 1782 not dominate the total CSM mass.

1783 The Type Ibn SN 2019uo is an exception: the observed pre-
 1784 cursor might have ejected $\sim 0.5 M_{\odot}$ of helium ~ 320 days
 1785 before the SN explosion. The low precursor luminosity is
 1786 expected if the material propagates through a low-density en-
 1787 vironment. If the material propagates with the CSM velocity
 1788 observed in the spectra it would remain confined to a rather
 1789 small radius. This would explain both the fast light-curve
 1790 evolution and the appearance of broad spectral features only
 1791 after 18 days after the explosion that indicate that the ejecta
 1792 have reached the edge of the optically thick CSM. It is hence
 1793 possible that the complete CSM of SN 2019uo is created dur-
 1794 ing the observed precursor, while the spectra and light curves
 1795 of the Type II_n SNe require earlier mass-loss events (see also
 1796 [Moriya & Maeda 2016](#)).

1797 Prior to Type II_n SNe, we only detect five precursors
 1798 that happen more than three months before core collapse (at
 1799 phases of 700 to 180 days before the explosion). At these
 1800 earlier times the rate (or duration) of bright precursors with
 1801 r -band magnitudes < -16 is lower by a factor of more than
 1802 10 and the rate of precursors brighter than magnitude -13 is
 1803 a factor of 5 lower. The increasing rate of bright precursors
 1804 could be explained if the precursors are powered by wave-
 1805 driven mass loss triggered by instabilities during the neon
 1806 and oxygen burning phases. [Shiode & Quataert \(2014\)](#) argue
 1807 that stars with lower core masses undergo fainter precursors
 1808 about a year before the SN explosion, while more massive
 1809 stellar cores produce brighter flares only weeks or days be-
 1810 fore core collapse, because of their shorter nuclear burning
 1811 phases. However, the most energetic precursor is 100 times
 1812 more energetic than predicted by [Shiode & Quataert \(2014\)](#),
 1813 and it is not clear whether energy transport to the stellar en-
 1814 velope could be as efficient.

1815 The bright outbursts shortly before the SN explosion open
 1816 the door to the possibility of predicting SN explosions. Four
 1817 of the precursors reach an apparent magnitude of < 20 (see
 1818 Figs. 3 and 4) and are potentially detectable with the ZTF dis-
 1819 covery pipeline. Based on these numbers, we estimate that
 1820 1–2 precursors per year are bright enough to allow the pre-

1821 diction of an imminent SN explosion. Indeed, the precursor
 1822 prior to SN 2019fmb was reported as a transient by the Pan-
 1823 STARRS collaboration ([Chambers et al. 2019](#)), but it was not
 1824 realized at the time that this was a pre-explosion outburst. We
 1825 conclude that the ZTF survey has the potential to predict SN
 1826 explosions if a dedicated search is implemented.

ACKNOWLEDGMENTS

1827 We thank A. Nyholm for his comments on the manuscript.
 1828 This work would not have been possible without the spec-
 1829 troscopic follow-up observations carried out by S. Anand,
 1830 D. Bektsev, N. Blagorodnova, M. Bulla, S. B. Cenko, W.
 1831 Chen, P. Chinchilla, R. Clavero Jimenez, C. Cunningham,
 1832 A. Dahiwal, L. Dominguez, A. J. Drake, C. Frohmaier, F.
 1833 J. Galindo-Guil, E. Hammerstein, T. Hung, N. Janssen, J.
 1834 Jenson, R. Karjalainen, H. Ko, M. Kuhn, E. McEwen, A.
 1835 A. Miller, S. Moran, M. C. Ramirez-Tannus, A. Smith, E.
 1836 Swann, K. Teet, J. Vinko, and J. Viuh. We would like to
 1837 thank participating observers on the UW APO ZTF follow-up
 1838 team, including Brigitta Spiócz, Eric Bellm, Zach Golkhou,
 1839 Keaton Bell, and James Davenport. In addition, we thank A.
 1840 Gangopadhyay, H. Ko, and S. Prentice for reducing optical
 1841 spectra and for sharing their data.

1842 Based on observations obtained with the 48-inch Samuel
 1843 Oschin Telescope and the 60-inch Telescope at Palomar Ob-
 1844 servatory as part of the Zwicky Transient Facility project.
 1845 ZTF is supported by the National Science Foundation
 1846 (NSF) under grant AST-1440341 and a collaboration in-
 1847 cluding Caltech, IPAC, the Weizmann Institute for Sci-
 1848 ence, the Oskar Klein Centre at Stockholm University,
 1849 the University of Maryland, the University of Washington,
 1850 Deutsches Elektronen-Synchrotron and Humboldt Univer-
 1851 sity, Los Alamos National Laboratories, the TANGO Consor-
 1852 tium of Taiwan, the University of Wisconsin at Milwaukee,
 1853 and the Lawrence Berkeley National Laboratory. Operations
 1854 are conducted by COO, IPAC, and UW. The SED Machine
 1855 is based upon work supported by NSF grant 1106171. This
 1856 work was supported by the GROWTH project funded by the
 1857 NSF under PIRE grant 1545949. Partially based on obser-
 1858 vations made with the Nordic Optical Telescope, operated
 1859 by the Nordic Optical Telescope Scientific Association at the
 1860 Observatorio del Roque de los Muchachos, La Palma, Spain,
 1861 of the Instituto de Astrofísica de Canarias. Some of the data
 1862 presented herein were obtained with ALFOSC. Some of the
 1863 data presented herein were obtained at the W. M. Keck Ob-
 1864 servatory, which is operated as a scientific partnership among
 1865 the California Institute of Technology, the University of Cal-
 1866 ifornia, and NASA; the observatory was made possible by
 1867 the generous financial support of the W. M. Keck Founda-
 1868 tion. The authors wish to recognize and acknowledge the

Table 6. SN Spectra

SN	obs. JD	instrument	time after t_0 (days)	line width (km s ⁻¹)	inst. res. (km s ⁻¹)	velocity (km s ⁻¹)	comment
SN 2018eru	2458351.7	P200/DBSP	35.0	1150	130	1143, 1000*	
SN 2018gho	2458372.7	P200/DBSP	6.2	400	130	378	
	2458383.4	LT/SPRAT	16.9	800	830	< 415	
SN 2018kag	2458470.5	LT/SPRAT	4.0	1150	830	796	
	2458502.5	NOT/ALFOSC	35.9	750	640	391	
	2458535.5	WHT/ACAM	68.9	1500	670	1342	broad
SN 2019uo	2458505.0	FTN/FLOYDS	3.7	–	–	990*	flash, He line
	2458506.9	FTN/FLOYDS	5.6	–	–	750*	
	2458508.3	LJT/YFOSC	7.0	–	–	850*	
	2458509.9	P200/DBSP	8.6	–	–	550*	
	2458519.9	FTN/FLOYDS	18.6	–	–	1200*	broad
	2458525.7	NOT/ALFOSC	24.4	–	–	1000*	broad
	2458529.2	LJT/YFOSC	27.9	–	–	1000*	broad
	2458579.9	Keck-1/LRIS	78.6	–	–	1000*	broad
SN 2019bxq	2458596.7	LT/SPRAT	40.8	900	830	< 415	
	2458598.0	P200/DBSP	42.1	330	130	303	
SN 2019cmy	2458572.8	APO/DIS	4.9	400	370	< 185	flash
	2458577.0	Keck-1/LRIS	9.1	350	320	< 160	
	2458580.9	APO/DIS	13.0	400	370	< 185	
	2458637.9	Keck-1/LRIS	70.0	400	320	240	broad
SN 2019iay	2458668.5	Lick 3-m/Kast	11.8	500	300	400	
	2458668.7	P200/DBSP	12.1	300	130	270	
SN 2019gjs	2458705.7	P200/DBSP	15.0	350	130	325	
SN 2019mom	2458705.9	P200/DBSP	14.9	450	130	431, 750*	
SN 2019fmb	2458792.0	APO/DIS	76.2	900	370	820	
	2458793.0	P200/DBSP	77.2	1000	130	992, 1050*	
SN 2019aafe	2458750.9	Keck-1/LRIS	10.1	1100	320	1052	
SN 2019vkl	2458812.1	Lijiang-2.4m/YFOSC	3.4	850	350	775	
SN 2019vts	2458834.8	APO/DIS	17.8	500	370	336	
SN 2019qny	2458853.4	LT/SPRAT	26.3	900	830	< 415	
SN 2020iq	2458898.8	Keck-1/LRIS	66.1	200	320	< 160 ^h	
SN 2019zrk	2458893.8	P200/DBSP	4.8	350	130	325 ^h	
	2458896.9	APO/DIS	7.8	400	370	< 185 ^h	
	2458896.6	LT/SPRAT	7.6	750	830	< 415 ^h	
	2458905.6	NOT/ALFOSC	16.6	800	640	480 ^h	
	2458930.9	Keck-1/LRIS	41.9	500	320	384 ^h	broad
SN 2020dcs	2458897.6	LT/SPRAT	2.7	850	830	< 415	
SN 2020dfh	2458906.9	ESO-NTT/EFOSC2	3.8	1000	980	< 490	
SN 2020edh	2458919.0	FTN/FLOYDS N-SIRAH	4.1	1000	800	600	

NOTE—List of SN spectra with narrow lines or P Cygni features. The typical resolution of the spectrograph (third column from the end) is subtracted from the measured width in quadrature, or we quote an upper limit if the result would be smaller than half the resolution. For most SNe, additional low-resolution spectra were obtained with the SED Machine.

Asterisks (*) mark velocities measured from P Cygni profiles and not from line widths. Spectra marked with an ^h have strong host lines such that the measured velocities are less reliable.

1869 very significant cultural role and reverence that the summit
1870 of Maunakea has always had within the indigenous Hawai-
1871 ian community. We are most fortunate to have the opportu-
1872 nity to conduct observations from this mountain. The Liv-
1873 erpool Telescope is operated on the island of La Palma by
1874 Liverpool John Moores University in the Spanish Observa-
1875 torio del Roque de los Muchachos of the Instituto de As-
1876 trofísica de Canarias with financial support from the UK Sci-
1877 ence and Technology Facilities Council. Research at Lick
1878 Observatory is partially supported by a generous gift from
1879 Google. The ztfquery code was funded by the European Re-
1880 search Council (ERC) under the European Union’s Horizon
1881 2020 research and innovation programme (grant agreement
1882 n759194 - USNAC, PI Rigault).

1883 E.O.O. is grateful for the support by grants from the Is-
1884 rael Science Foundation, Minerva, Israeli Ministry of Tech-
1885 nology and Science, the US-Israel Binational Science Founda-
1886 tion, Weizmann-UK, Weizmann-Yale, and the Weizmann-
1887 Caltech grants. A.G.Y.’s research is supported by the EU
1888 via ERC grant 725161, the ISF GW excellence center, an
1889 IMOS space infrastructure grant and BSF/Transformative

1890 and GIF grants, as well as The Benozio Endowment Fund
1891 for the Advancement of Science, the Deloro Institute for Ad-
1892 vanced Research in Space and Optics, The Veronika A. Rabl
1893 Physics Discretionary Fund, Paul and Tina Gardner, Yeda-
1894 Sela and the WIS-CIT joint research grant; A.G.Y. is the
1895 recipient of the Helen and Martin Kimmel Award for In-
1896 novative Investigation. N.J.S. is grateful for the support by
1897 the ISF (grant 1770/19). A.V.F. acknowledges support from
1898 the Christopher R. Redlich Fund, the TABASGO Founda-
1899 tion, and the Miller Institute for Basic Research in Science.
1900 L.T. acknowledges support from MIUR (PRIN 2017 grant
1901 20179ZF5KS). R.L. is supported by a Marie Skłodowska-
1902 Curie Individual Fellowship within the Horizon 2020 Euro-
1903 pean Union (EU) Framework Programme for Research and
1904 Innovation (H2020-MSCA-IF-2017-794467). M.L.G. ac-
1905 knowledges support from the DiRAC Institute in the Depart-
1906 ment of Astronomy at the University of Washington. The
1907 DiRAC Institute is supported through generous gifts from
1908 the Charles and Lisa Simonyi Fund for Arts and Sciences,
1909 and the Washington Research Foundation.

REFERENCES

- 1910 Ahumada, R., Prieto, C. A., Almeida, A., et al. 2019, The Sixteenth
1911 Data Release of the Sloan Digital Sky Surveys: First Release
1912 from the APOGEE-2 Southern Survey and Full Release of
1913 eBOSS Spectra
- 1914 Arnett, W. D. & Meakin, C. 2011a, *ApJ*, 733, 78
- 1915 Arnett, W. D. & Meakin, C. 2011b, *ApJ*, 741, 33
- 1916 Bellm, E. C., Kulkarni, S. R., Graham, M. J., et al. 2019, *PASP*,
1917 131, 018002
- 1918 Ben-Ami, S., Konidaris, N., Quimby, R., et al. 2012, in *Society of*
1919 *Photo-Optical Instrumentation Engineers (SPIE) Conference*
1920 *Series*, Vol. 8446, Ground-based and Airborne Instrumentation
1921 for Astronomy IV, 844686
- 1922 Bertin, E., Mellier, Y., Radovich, M., et al. 2002, in *Astronomical*
1923 *Society of the Pacific Conference Series*, Vol. 281, *Astronomical*
1924 *Data Analysis Software and Systems XI*, ed. D. A. Bohlender,
1925 D. Durand, & T. H. Handley, 228
- 1926 Bilinski, C., Smith, N., Li, W., et al. 2015, *MNRAS*, 450, 246
- 1927 Blagorodnova, N., Neill, J. D., Walters, R., et al. 2018, *PASP*, 130,
1928 035003
- 1929 Bruch, R. J., Gal-Yam, A., Schulze, S., et al. 2020, *arXiv e-prints*,
1930 *arXiv:2008.09986*
- 1931 Cardelli, J. A., Clayton, G. C., & Mathis, J. S. 1989, *ApJ*, 345, 245
- 1932 Chambers, K. C., Boer, T. D., Bulger, J., et al. 2019, *Transient*
1933 *Name Server Discovery Report*, 2019-796, 1
- 1934 Chevalier, R. A. & Irwin, C. M. 2011, *ApJL*, 729, L6
- 1935 Cutri, R. M., Wright, E. L., Conrow, T., et al. 2013, *Explanatory*
1936 *Supplement to the AllWISE Data Release Products*, *Explanatory*
1937 *Supplement to the AllWISE Data Release Products*
- 1938 Danieli, B. & Soker, N. 2019, *MNRAS*, 482, 2277
- 1939 Dilday, B., Howell, D. A., Cenko, S. B., et al. 2012, *Science*, 337,
1940 942
- 1941 Duev, D. A., Mahabal, A., Masci, F. J., et al. 2019, *MNRAS*, 489,
1942 3582
- 1943 Elias-Rosa, N., Pastorello, A., Benetti, S., et al. 2016, *MNRAS*,
1944 463, 3894
- 1945 Filippenko, A. V. 1997, *ARA&A*, 35, 309
- 1946 Finkbeiner, D. P., Padmanabhan, N., Schlegel, D. J., et al. 2004,
1947 *AJ*, 128, 2577
- 1948 Foley, R. J., Berger, E., Fox, O., et al. 2011, *ApJ*, 732, 32
- 1949 Foley, R. J., Smith, N., Ganeshalingam, M., et al. 2007, *ApJL*, 657,
1950 L105
- 1951 Fraser, M., Magee, M., Kotak, R., et al. 2013, *ApJL*, 779, L8
- 1952 Fremling, C., Dugas, A., & Sharma, Y. 2019, *Transient Name*
1953 *Server Classification Report*, 2019-188, 1
- 1954 Fremling, C., Miller, A. A., Sharma, Y., et al. 2020, *ApJ*, 895, 32
- 1955 Fuller, J. 2017, *MNRAS*, 470, 1642
- 1956 Gal-Yam, A. 2017, *Handbook of Supernovae*, 195–237
- 1957 Gal-Yam, A. 2019, in *American Astronomical Society Meeting*
1958 *Abstracts*, Vol. 233, *American Astronomical Society Meeting*
1959 *Abstracts #233*, 131.06
- 1960 Gal-Yam, A. 2019, *ARA&A*, 57, 305–333
- 1961 Gal-Yam, A., Arcavi, I., Ofek, E. O., et al. 2014, *Nature*, 509, 471

- Gal-Yam, A. & Leonard, D. C. 2009, *Nature*, 458, 865
- Gal-Yam, A., Leonard, D. C., Fox, D. B., et al. 2007, *ApJ*, 656, 372
- Gangopadhyay, A., Misra, K., Hiramatsu, D., et al. 2020, *ApJ*, 889, 170
- Ginzburg, S. & Balberg, S. 2012, *ApJ*, 757, 178
- Glas, R., Just, O., Janka, H. T., & Obergaulinger, M. 2019, *ApJ*, 873, 45
- Graham, M. J., Kulkarni, S. R., Bellm, E. C., et al. 2019, *PASP*, 131, 078001
- Hamuy, M., Phillips, M. M., Suntzeff, N. B., et al. 2003, *Nature*, 424, 651
- Ho, A. Y. Q., Goldstein, D. A., Schulze, S., et al. 2019, *ApJ*, 887, 169
- Hosseinzadeh, G., Arcavi, I., Valenti, S., et al. 2017, *ApJ*, 836, 158
- Hosseinzadeh, G., McCully, C., Zabludoff, A. I., et al. 2019, *ApJ*, 871, L9
- Humphreys, R. M. & Davidson, K. 1994, *PASP*, 106, 1025
- Janka, H.-T., Melson, T., & Summa, A. 2016, *Annual Review of Nuclear and Particle Science*, 66, 341
- Karamahmetoglu, E., Fransson, C., Sollerman, J., et al. 2019, arXiv e-prints, arXiv:1910.06016
- Kasliwal, M. M., Cannella, C., Bagdasaryan, A., et al. 2019, *PASP*, 131, 038003
- Katz, B., Sapir, N., & Waxman, E. 2011, arXiv e-prints, arXiv:1106.1898
- Khazov, D., Yaron, O., Gal-Yam, A., et al. 2016, *ApJ*, 818, 3
- Kiewe, M., Gal-Yam, A., Arcavi, I., et al. 2012, *ApJ*, 744, 10
- Kochanek, C. S. & Szczygiel, D. M. 2011, *ApJ*, 737, 76
- Kool, E. C., Karamahmetoglu, E., Sollerman, J., et al. 2020, arXiv e-prints, arXiv:2008.04056
- Law, N. M., Kulkarni, S. R., Dekany, R. G., et al. 2009, *PASP*, 121, 1395
- Liu, X., Shen, Y., Strauss, M. A., & Hao, L. 2011, *ApJ*, 737, 101
- Lupton, R. H., Gunn, J. E., & Szalay, A. S. 1999, *AJ*, 118, 1406
- Malmquist, K. G. 1922, *Meddelanden fran Lunds Astronomiska Observatorium Serie I*, 100, 1
- Margutti, R., Kamble, A., Milisavljevic, D., et al. 2017, *ApJ*, 835, 140
- Margutti, R., Milisavljevic, D., Soderberg, A. M., et al. 2013, *ApJ*, 780, 21
- Masci, F. J., Laher, R. R., Rusholme, B., et al. 2019, *PASP*, 131, 018003
- Mauerhan, J. C., Smith, N., Filippenko, A. V., et al. 2013, *MNRAS*, 430, 1801
- Mcley, L. & Soker, N. 2014, *MNRAS*, 445, 2492
- Meakin, C. A. & Arnett, D. 2006, *ApJL*, 637, L53
- Moriya, T. J. 2014, *A&A*, 564, A83
- Moriya, T. J. 2015, *The Astrophysical Journal*, 803, L26
- Moriya, T. J. & Maeda, K. 2016, *ApJ*, 824, 100
- Moriya, T. J., Maeda, K., Taddia, F., et al. 2014, *MNRAS*, 439, 2917
- Müller, B. 2016, *PASA*, 33, e048
- Murase, K., Thompson, T. A., Lacki, B. C., & Beacom, J. F. 2011, *PhRvD*, 84, 043003
- Murase, K., Thompson, T. A., & Ofek, E. O. 2014, *MNRAS*, 440, 2528
- Nordin, J., Brinnel, V., van Santen, J., et al. 2019, *A&A*, 631, A147
- Nyholm, A., Sollerman, J., Taddia, F., et al. 2017, *Astronomy Astrophysics*, 605, A6
- Nyholm, A., Sollerman, J., Tartaglia, L., et al. 2020, *Astronomy Astrophysics*, 637, A73
- Ofek, E. O. 2019, *PASP*, 131, 054504
- Ofek, E. O., Cenko, S. B., Shaviv, N. J., et al. 2016, *ApJ*, 824, 6
- Ofek, E. O., Lin, L., Kouveliotou, C., et al. 2013a, *ApJ*, 768, 47
- Ofek, E. O., Rabinak, I., Neill, J. D., et al. 2010, *ApJ*, 724, 1396
- Ofek, E. O., Sullivan, M., Cenko, S. B., et al. 2013b, *Nature*, 494, 65
- Ofek, E. O., Sullivan, M., Shaviv, N. J., et al. 2014a, *ApJ*, 789, 104
- Ofek, E. O., Zoglauer, A., Boggs, S. E., et al. 2014b, *ApJ*, 781, 42
- Osborn, J., Föhning, D., Dhillon, V. S., & Wilson, R. W. 2015, *MNRAS*, 452, 1707
- Owocki, S. P., Hirai, R., Podsiadlowski, P., & Schneider, F. R. N. 2019, *MNRAS*, 485, 988
- Owocki, S. P. & Shaviv, N. J. 2016, *MNRAS*, 462, 345
- Pastorello, A., Cappellaro, E., Inserra, C., et al. 2013, *ApJ*, 767, 1
- Pastorello, A., Kochanek, C. S., Fraser, M., et al. 2018, *MNRAS*, 474, 197
- Pastorello, A., Smartt, S. J., Mattila, S., et al. 2007, *Nature*, 447, 829
- Pastorello, A., Wang, X. F., Ciabattari, F., et al. 2016, *MNRAS*, 456, 853
- Patat, F., Taubenberger, S., Benetti, S., Pastorello, A., & Harutyunyan, A. 2011, *A&A*, 527, L6
- Patterson, M. T., Bellm, E. C., Rusholme, B., et al. 2019, *PASP*, 131, 018001
- Paxton, B., Bildsten, L., Dotter, A., et al. 2011, *ApJS*, 192, 3
- Perley, D. A., Fremling, C., Sollerman, J., et al. 2020, arXiv e-prints, arXiv:2009.01242
- Piro, A. L. & Nakar, E. 2013, *ApJ*, 769, 67
- Price-Whelan, A. M., Sipőcz, B. M., Günther, H. M., et al. 2018, *AJ*, 156, 123
- Prieto, J. L., Brimacombe, J., Drake, A. J., & Howerton, S. 2013, *ApJ*, 763, L27
- Quataert, E., Fernández, R., Kasen, D., Klion, H., & Paxton, B. 2016, *MNRAS*, 458, 1214
- Quataert, E. & Shiode, J. 2012, *MNRAS*, 423, L92
- Rau, A., Kulkarni, S. R., Law, N. M., et al. 2009, *PASP*, 121, 1334
- Reguitti, A., Pastorello, A., Pignata, G., et al. 2019, *MNRAS*, 482, 2750

- 2061 Rest, A., Prieto, J. L., Walborn, N. R., et al. 2012, *Nature*, 482, 375
- 2062 Rigault, M. 2018, *ztfquery*, a python tool to access ZTF data
- 2063 Rigault, M., Neill, J. D., Blagorodnova, N., et al. 2019, *A&A*, 627,
2064 A115
- 2065 Robitaille, T. P., Tollerud, E. J., Greenfield, P., et al. 2013, *A&A*,
2066 558, A33
- 2067 Sanders, N. E., Soderberg, A. M., Foley, R. J., et al. 2013, *ApJ*,
2068 769, 39
- 2069 Sapir, N. & Waxman, E. 2017, *ApJ*, 838, 130
- 2070 Schlafly, E. F. & Finkbeiner, D. P. 2011, *ApJ*, 737, 103
- 2071 Schlegel, D. J., Finkbeiner, D. P., & Davis, M. 1998, *ApJ*, 500, 525
- 2072 Shaviv, N. J. 2000, *ApJL*, 532, L137
- 2073 Shaviv, N. J. 2001a, *ApJ*, 549, 1093
- 2074 Shaviv, N. J. 2001b, *MNRAS*, 326, 126
- 2075 Shiode, J. H. & Quataert, E. 2014, *ApJ*, 780, 96
- 2076 Silverman, J. M., Nugent, P. E., Gal-Yam, A., et al. 2013, *ApJS*,
2077 207, 3
- 2078 Smith, N. 2017, *Handbook of Supernovae*, 403–429
- 2079 Smith, N. 2017, *Philosophical Transactions of the Royal Society of*
2080 *London Series A*, 375, 20160268
- 2081 Smith, N. & Arnett, W. D. 2014, *ApJ*, 785, 82
- 2082 Smith, N., E Andrews, J., Moe, M., et al. 2020, *MNRAS*, 492, 5897
- 2083 Smith, N., Mauerhan, J. C., Silverman, J. M., et al. 2012, *MNRAS*,
2084 426, 1905
- 2085 Smith, N., Vink, J. S., & de Koter, A. 2004, *ApJ*, 615, 475
- 2086 Soumagnac, M. T. & Ofek, E. O. 2018, *PASP*, 130, 075002
- 2087 Soumagnac, M. T., Ofek, E. O., Gal-Yam, A., et al. 2019, *ApJ*,
2088 872, 141
- 2089 Soumagnac, M. T., Ofek, E. O., Liang, J., et al. 2020, *ApJ*, 899, 51
- 2090 Stritzinger, M., Taddia, F., Fransson, C., et al. 2012, *ApJ*, 756, 173
- 2091 Strotjohann, N. L., Ofek, E. O., Gal-Yam, A., et al. 2015, *ApJ*, 811,
2092 117
- 2093 Svirski, G., Nakar, E., & Sari, R. 2012, *ApJ*, 759, 108
- 2094 Tartaglia, L., Pastorello, A., Sullivan, M., et al. 2016, *MNRAS*,
2095 459, 1039
- 2096 Thöne, C. C., de Ugarte Postigo, A., Leloudas, G., et al. 2017,
2097 *A&A*, 599, A129
- 2098 Wallis, S. 2013, *Journal of Quantitative Linguistics*, 20, 178
- 2099 Wilson, E. B. 1927, *Journal of the American Statistical*
2100 *Association*, 22, 209
- 2101 Woosley, S. E. 2017, *ApJ*, 836, 244
- 2102 Woosley, S. E., Heger, A., & Weaver, T. A. 2002, *Reviews of*
2103 *Modern Physics*, 74, 1015
- 2104 Yao, Y., Miller, A. A., Kulkarni, S. R., et al. 2019, *ApJ*, 886, 152
- 2105 Yaron, O., Perley, D. A., Gal-Yam, A., et al. 2017, *Nature Physics*,
2106 13, 510–517
- 2107 Zackay, B., Ofek, E. O., & Gal-Yam, A. 2016, *ApJ*, 830, 27

2108

APPENDIX

2109

A. PRECURSOR IMAGES

2110 To test whether the precursor candidates are real, we inspect the difference images. We select either the g or r band and coadd
 2111 the difference images that yield the most significant fluxes in our search (see Figs. 3 and 4). Before the coaddition we subtract the
 2112 median pixel flux from the image and divide all fluxes by the robust standard deviation (half of the difference between the 15.9%
 2113 and 84.1% percentile). The images are then coadded using the *SWarp* software (Bertin et al. 2002). The resulting skymaps are
 2114 shown in Fig. 15. Clear point sources are visible for most SNe.

2115 To quantify the significance of the detections in Fig. 15, we calculate the S-image as described by Zackay et al. (2016). For
 2116 this purpose, we cross correlate the difference image with the PSF of the difference image and coadd the resulting significance
 2117 maps again using *SWarp*. To normalize the significances we divide each image by the robust standard deviation and show the
 2118 significance maps in Fig. 16.

2119 Most precursors are visible as point sources, with exception of SN 2019sae. This precursor candidate is considered unconfirmed
 2120 as only a single bin drives the significance (compare Sec. 3.1) and we conclude that it is likely spurious. The other three
 2121 unconfirmed precursors (marked by red titles in Figs. 15 and 16) appear as point sources, so we cannot rule out that they are
 2122 astrophysical. As described in Sec. 3.1 we neglect these marginal detections here and only focus on the 19 confirmed precursors.
 2123 In some cases astrometric residuals are visible in the cutouts close to the precursors. Especially affected are SN 2018gho and
 2124 SN 2020dfh. We nevertheless consider them true detections as they also appear to be present in single images without astrometric
 2125 residuals. We caution however that their light curves could be affected by the missubtractions. They are therefore less reliable
 2126 than the light curves of other precursors.

2127

B. BASELINE CORRECTION OF SN 2019CMY

2128 When using late-time observations (> 380 days after the explosion) for the baseline correction of SN 2019cmy, we find that the
 2129 complete pre-explosion light curve becomes positive as shown in Fig. 17. The late-time observations include > 60 observations
 2130 per filter collected in > 30 different nights over a period of 50 days. They are consistent with a constant flux, which is however
 2131 $\sim 10^{-9}$ lower than the median flux before the explosion. To probe whether a systematic error could explain this deviation we
 2132 perform a series of tests: The hour angle and air mass are on average similar before and after the explosion. The seeing is better
 2133 during the last block of observations collected since March 2020, potentially because of reduced air pollution as a consequence
 2134 of the lockdown measures due to the Corona pandemic. However, other SNe in our sample do not show a similarly strong flux
 2135 change, implying that we do not see a global effect caused by changes in the atmosphere.

2136 The pixel coordinates of the SN position drift slowly by in total 100 pixels over three years, but there is no abrupt change
 2137 consistent with the two different flux levels. We also inspect the mirrored SN position, located at a distance of 11.2 arcsec on the
 2138 other side of the host galaxy's center. We observe a constant flux level for the complete light curve, i.e. a similar flux reduction is
 2139 not observed at late times. Finally, we use the ZUDS pipeline to construct a different reference image, redo the image subtraction
 2140 and produce a forced photometry light curve. The flux difference between the observations before and after the explosion is
 2141 similarly large. It is therefore likely not induced by the image subtraction or forced photometry pipeline.

2142 After we could not identify any systematic effect responsible for the lower fluxes after the SN has faded, we here discuss an
 2143 astrophysical interpretation. If real, the flux drop would imply that the progenitor star is detected for 400 days before the SN
 2144 explosion. A flux of 10^{-9} corresponds to a magnitude of 22.5, i.e. and absolute magnitude of -14.1 for the SN redshift of 0.0314.
 2145 The detected progenitor star prior to SN 2005gl had a V band magnitude of only -10.4 (Gal-Yam & Leonard 2009), but we
 2146 cannot rule out that the progenitor underwent a more than year-long outburst with an approximately constant luminosity. Similar
 2147 outbursts were observed several years prior to the explosion of SN 2015bh and reached typical r -band magnitudes between -9
 2148 and -13 (Elias-Rosa et al. 2016; Thöne et al. 2017). It is thus not excluded that we indeed detect the progenitor star.

2149 Since we are not sure whether or not the flux reduction after the SN explosion is astrophysical, we here exclude the late-time
 2150 observations and do the baseline correction using pre-explosion data. r -band observations in two nights, 7 and 6 days before the
 2151 estimated explosion date surpass the 5σ detection as shown in Fig. 3. They could either be a precursor eruption or a wind-shock
 2152 breakout peak (Ofek et al. 2010; Chevalier & Irwin 2011; Piro & Nakar 2013).

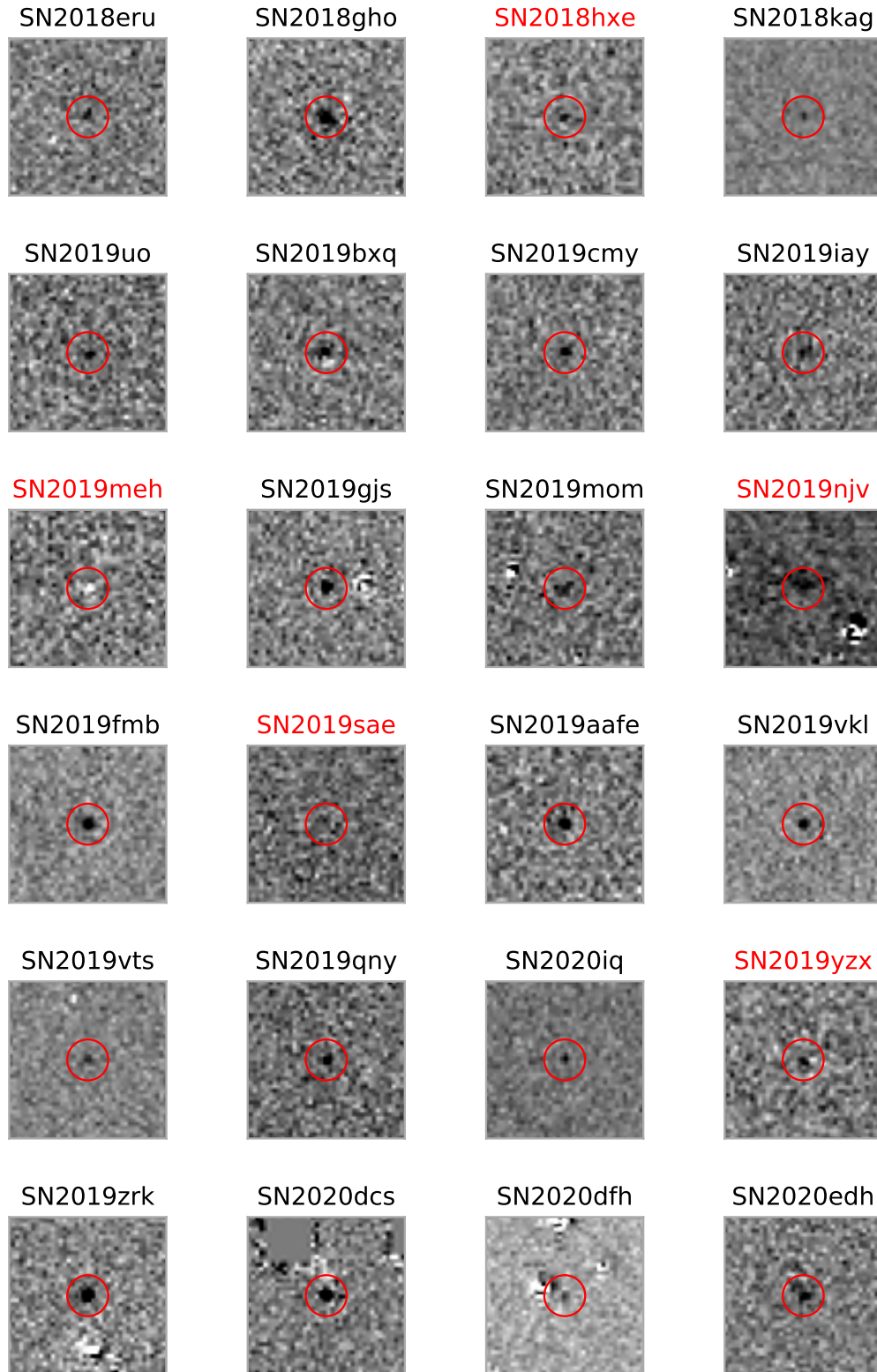


Figure 15. Coadded ZTF difference images showing the precursors. Red captions indicate that the corresponding precursor is only detected in a single bin and is therefore considered unconfirmed (see Sec. 3.1). No point source is visible for SN 2019sae and we conclude that this precursor candidate is not real. A negative source is detected at the position of SN 2019meh due to the AGN variability in the host galaxy.

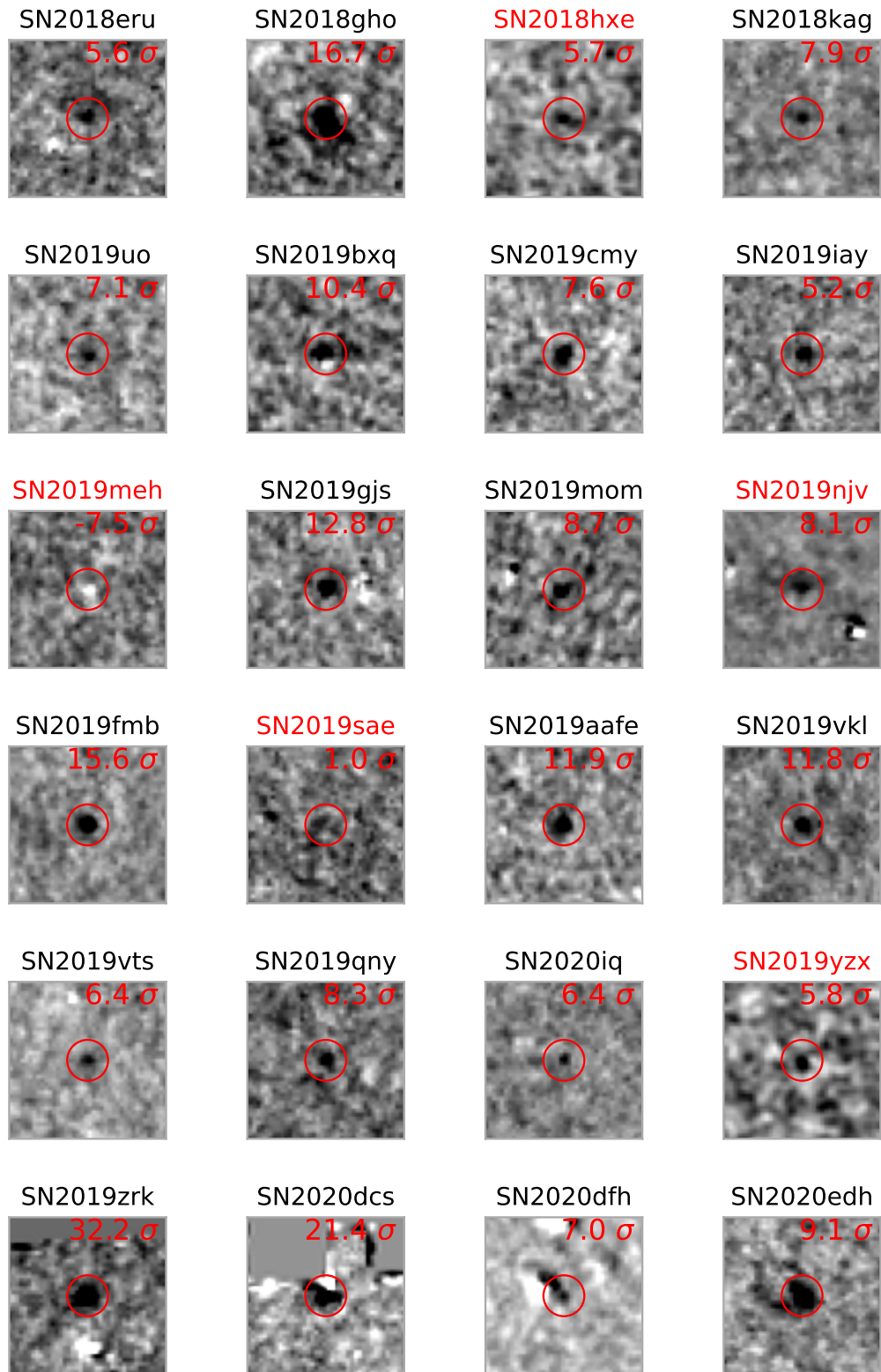


Figure 16. Significance maps of the precursor candidates.

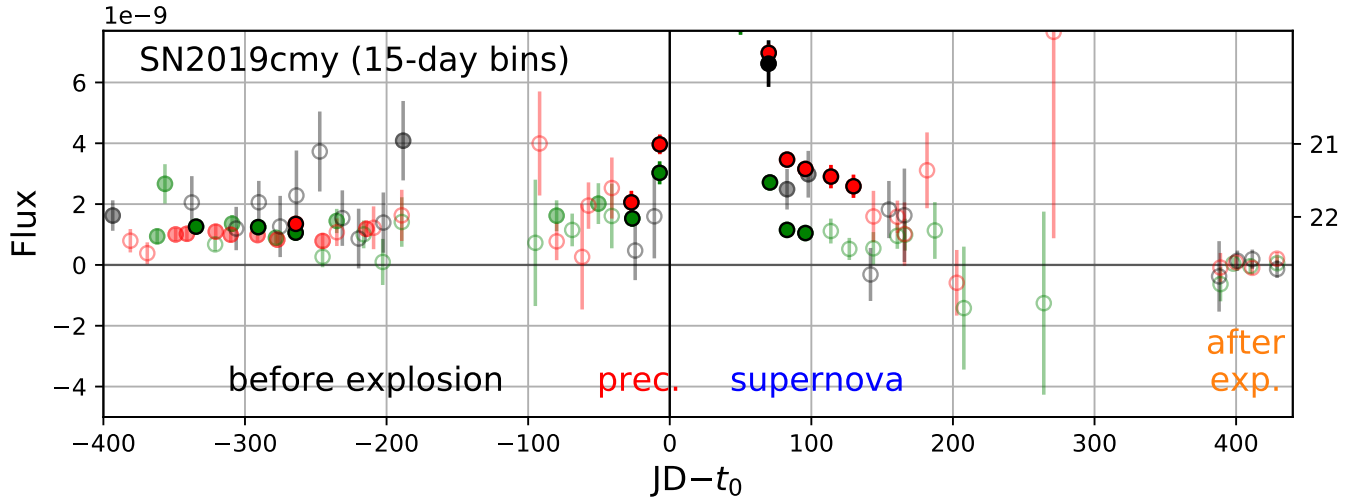


Figure 17. Complete light curve for the position of SN2019cmy when using the last observations (yellow region) for the baseline correction. The peak of the SN is cut for better visibility. The complete pre-explosion light curve (gray region) is positive, i.e. the fluxes before and after the SN cannot be zero at the same time. We could not identify a systematic effect that might explain this discrepancy. If the effect is astrophysical, it would imply that the progenitor star is detected with an absolute magnitude of -14.1 . In this paper, we use pre-explosion observations for the baseline correction and only discuss the precursor detected one week before the SN (red region).